

Molecular Dynamics Simulations of Precursor-Derived Si-C-N Ceramics

Von der Fakultät Chemie der Universität Stuttgart
zur Erlangung der Würde eines
Doktors der Naturwissenschaften (Dr. rer. nat.)
genehmigte Abhandlung

vorgelegt von
Nicoletta Resta
aus Trieste, Italien

Hauptberichter : Prof. Dr. Hans-Rainer Trebin
Mitberichter : Prof. Dr. Fritz Aldinger
Mitprüfer : Prof. Dr. ir. Eric Mittemeijer

Tag der mündlichen Prüfung : 8 Juni 2005

Max-Planck-Institut für Metallforschung
Stuttgart
und
Institut für Theoretische und Angewandte Physik
Universität Stuttgart

2005

Contents

Abstract	iii
Zusammenfassung und Ausblick	
<i>Extended abstract and outlook in german</i>	v
1 Introduction	1
2 Precursor-Derived Si-C-N Ceramics	5
2.1 Preparation of the Amorphous Ceramic	6
2.2 High temperature behavior	9
2.3 Applications	11
3 Modeling of Covalent Ceramics by Molecular Dynamics	15
3.1 Thermodynamic and structural properties	16
3.1.1 Temperature and pressure	18
3.1.2 Distribution functions	19
3.2 Modeling covalent materials	20
3.2.1 The Tersoff Potential	22
4 Simulations of amorphous Si-C-N	27
4.1 Modification of the Tersoff Potential	28
4.2 Calculation of distribution functions	28
4.3 Dependence of the Atomic Structure on the Chemical Composition	30
4.3.1 Method	30
4.3.2 Results of simulations	31
4.3.3 Summary	42
4.4 Thermal Evolution	45
4.4.1 Method	45
4.4.2 Energy and density during annealing at high T	46
4.4.3 Self-diffusion in amorphous Si-C-N	48
4.4.4 Structural evolution	51
4.4.5 Summary	58
5 Simulations of crystal growth	61
5.1 Crystal growth of diamond	61
5.1.1 Method	62

5.1.2	Annealing at different temperatures	62
5.1.3	Diamond crystal seed with twin grain boundaries .	64
5.1.4	Different shapes of the diamond seed	66
5.1.5	Summary	67
5.2	Crystal growth of cubic SiC	69
5.2.1	Method	69
5.2.2	Results	71
5.2.3	Summary	73
6	Conclusions and Outlook	75
	Appendix	79
A	Verlet algorithm	79
B	Tersoff Potential	81
	Bibliography	91
	Acknowledgments	99
	Curriculum Vitae	101

Abstract

The microscopic mechanisms behind the transformation from the amorphous Si-C-N ceramics to the polycrystalline material are studied by isolating its fundamental steps. Si-C-N amorphous ceramics, amorphous and crystalline silicon carbide, and carbon, are numerically modeled by means of classical molecular dynamics. The interatomic interactions are modeled by the Tersoff many-body empirical potential.

In the first part amorphous Si-C-N materials are studied. We show how the atomic structures of these ceramics depend on their chemical composition. Amorphous systems are obtained by rapid cooling from high temperatures. We find that the atomic structures depend on the relative concentration of silicon and nitrogen, regardless of the carbon amount. In particular, for a stoichiometric nitrogen/silicon ratio $\geq 4/3$, the atoms separate into two amorphous phases, a sp^2 hybridized C-rich, and a Si/N-rich one. In this phase, silicon atoms form mainly SiN_4 and mixed $Si(C,N)_4$ tetrahedra. Far above the $4/3$ ratio, we find Si/N-rich domains, where Si atoms are more than four-fold coordinated, and are surrounded by graphitic monolayers. In another set of simulations, the thermal evolution of a Si-C-N system is followed by annealing it at high temperatures. Volume shrinkage of $\simeq 12\%$ is observed and diffusion activation energies of 3.43 eV for Si, 3.63 eV for C, and 2.94 eV for N are calculated. We find that carbon atoms are the slowest atomic species in the amorphous network.

In the second part of this work we study the crystal growth of silicon carbide from the amorphous phase. In a preliminary set of simulations, the study of diamond crystal growth demonstrates that empirical potentials can predict crystallization processes in complex covalent compounds. The crystal growth of a seed of cubic SiC into the amorphous material is then investigated. The dependence of the growth process on the crystallographic orientation of the crystalline/amorphous interface is studied by considering three different crystal planes, namely the $\{100\}$, $\{110\}$, and $\{111\}$ planes. We observe the crystal growth only for the $\{110\}$ and the $\{111\}$ orientations, but not for the $\{100\}$ ones. All interfaces after the annealing have a common atomic structure: Silicon $\{111\}$ layers, triple bonded to the bulk. Moreover, we find that the preferential growth directions are the $\langle 110 \rangle$ ones, perpendicular to the $\{110\}$ surfaces. Crystal growth proceeds by faceting on the $\{111\}$ planes.

Zusammenfassung und Ausblick

Extended abstract and outlook in german

Silizium-Kohlenstoff-Stickstoff (Si-C-N)-Keramiken sind kovalente Nichtoxid-Keramiken, die sich durch eine einzigartige thermische, chemische und mechanische Stabilität auszeichnen. Diese Eigenschaften machen sie zu geeigneten Kandidaten für den Hochtemperatureinsatz in Motoren- und Gasturbinenbauteilen.

Ein Verfahren zur Herstellung dieser kovalenten Keramiken stellt die thermische Zersetzung von metall-organischen Prekursor-Polymeren dar. Dieser Prozess führt zu oxidfreien amorphen Si-C-N-Keramiken, die bis in den atomaren Bereich homogen sind. Darüber hinaus kann das Gefüge bis zu einem gewissen Grade durch die Wahl geeigneter Polymer-Prekursoren bestimmt werden.

Wegen der geringen Beweglichkeit der drei atomaren Bestandteile bleiben Si-C-N-Keramiken bis zu hohen Temperaturen von $T \simeq 1800$ K in ihrem amorphen Zustand. Vermutlich sind diese Materialien auch deshalb thermisch, chemisch und mechanisch stabil. Wenn aber die Si-C-N-Materialien bei hohen Temperaturen angelassen werden, gehen schließlich viele wünschenswerte Eigenschaften dieser amorphen Keramiken verloren. In der Tat erfolgt ein Übergang in die thermodynamisch stabilen Phasen Graphit, α -Si₃N₄, β -SiC und gasförmiges N₂, wobei das amorphe Netzwerk zerstört wird. Die beobachtete Volumenabnahme und Rissbildung in Si-C-N-Keramiken können auf Kristallisationsprozesse zurückgeführt werden. Der Mechanismus dieses Phasenüberganges ist immer noch nicht ganz verstanden. Es wird angenommen, dass er aus einer schrittweisen Änderung des Gefüges besteht, die — eingeleitet durch eine Umordnung der Polymer-Netzwerkstruktur während der Wärmebehandlung — zu einer Phasenseparation in Domänen führt, die reich an Kohlenstoff, Silizium/Stickstoff bzw. Silizium/Kohlenstoff sind. Die Änderung in den lokalen chemischen Verhältnissen und die Bildung der Gasphase (Entweichen von N₂-Molekülen) unterstützen äußere und innere Kristallisation der jeweiligen Phasen, d. h. von Graphit, Siliziumnitrid (α -Si₃N₄) und kubischem Siliziumkarbid (β -SiC).

In der vorliegenden Arbeit wurden die mikroskopischen Vorgänge, die dem Übergang von der amorphen Keramik zum polykristallinen Material zugrundeliegen, untersucht, indem die entscheidenden Schritte getrennt betrachtet wurden. Diese Teilschritte umfassen die atomistische Struktur der Si-C-N-Keramiken im Zustand ihrer Entstehung, ihre thermische Entwicklung und schließlich ihre Kristallisation. Das Ziel dieser Arbeit war es, Erkenntnisse über diese Phänomene auf atomarem Niveau zu gewinnen.

Si-C-N-Materialien wurden numerisch durch die klassische Molekulardynamik (MD) modelliert, bei der die interatomaren Wechselwirkungen gemäß der newtonischen Mechanik beschrieben werden. Tatsächlich gehen die Zeit- und Längenskalen der untersuchten Vorgänge über die Möglichkeiten der *ab initio*-Berechnungen hinaus, bei denen quantenmechanische Effekte berücksichtigt werden. Die Wahl der klassischen MD ist daher durch die Probleme bestimmt. Dies schließt die Verwendung von empirischen Potenzialen zur Beschreibung der interatomaren Wechselwirkungen ein. Für vorwiegend kovalent gebundene Materialien wie Si-C-N ist das beste verfügbare empirische Potenzial das von J. Tersoff entwickelte, das auf dem Konzept der *bond order* beruht. Die potenzielle Energie wird als Summe von Paarwechselwirkungen beschrieben, wobei jedoch der Vorfaktor des attraktiven Anteils, der die Rolle der *bond order* spielt, von der lokalen Umgebung der Atompaare abhängt und auf diese Weise zu einem Mehrkörperpotenzial führt.

Diese Arbeit ist in zwei Teile gegliedert. Der erste befasst sich mit der Simulation der amorphen Si-C-N-Strukturen, der zweite mit dem Kristallwachstum von kubischem SiC.

Im ersten Teil wurde die atomare Struktur der homogenen Si-C-N-Materialien mit verschiedenen Zusammensetzungen simuliert und dann die thermische Entwicklung eines bestimmten Systems, das dem experimentellen System VT50 entspricht, betrachtet. Obwohl leistungsfähige Analysemethoden zur Verfügung stehen, ist das Gefüge der amorphen Si-C-N-Keramiken nicht vollständig bekannt. Insbesondere stellt sich die Frage, ob eine Phasenseparation in amorphen Domänen bereits in den hergestellten Keramiken auftritt oder ob die Phasenseparation eine Folge von nachfolgender Wärmebehandlung ist. Dies ist eine wichtige

Frage, denn die Phasenseparation ist der erste Schritt in Richtung auf eine Zersetzung der Keramiken bei hoher Temperatur.

Experimentell kann man Si-C-N Keramiken in weiten Grenzen mit einer gewünschten chemischen Zusammensetzung herstellen. In der vorliegenden Arbeit sollte der Einfluss der Zusammensetzung auf das Gefüge untersucht werden. Zu diesem Zweck wurden die atomaren Strukturen von verschiedenen Si-C-N-Systemen simuliert. Die Ergebnisse stimmen mit den experimentellen Resultaten überein und können folgendermaßen zusammengefasst werden:

- (i) Die lokale Struktur in der Umgebung von Siliziumatomen hängt — unabhängig von der Kohlenstoffkonzentration — vom Stickstoff/Silizium-Verhältnis ab. Im Allgemeinen stellt man fest, dass stets gemischte $\text{Si}(\text{C},\text{N})_4$ Tetraeder vorliegen. Für ein N/Si-Verhältnis um 4/3 beobachtet man eine Phasentrennung in eine amorphe Si_3N_4 -reiche Phase was experimentell nachgewiesen wurde.
- (ii) Kohlenstoff ist immer im Mittel dreifach koordiniert und liegt in gemischten planaren $\text{C}(\text{Si},\text{C})_3$ -Strukturen vor. Die lokale Struktur in der Umgebung von Kohlenstoff hängt von der Menge des zur Verfügung stehenden Siliziums ab, das heißt der nicht durch Stickstoff abgeschirmten Siliziumatome. Es werden sp^2 C-reiche Domänen beobachtet, wenn das Verhältnis C/Si groß genug ist. Im extremen Fall, wenn kein verfügbares Silizium vorhanden ist, d.h. wenn Silizium vollständig durch N abgeschirmt wird, bilden sich graphitische Monolagen innerhalb des Materials.

Anschließend wurde die thermische Entwicklung eines ausgewählten Si-C-N-Systems simuliert. Die potentielle Energie, die Dichte und die Diffusionskoeffizienten wurden während des Erhitzens von Raumtemperatur bis zu sehr hohen Temperaturen von $T \simeq 4000$ K untersucht. Ein Minimum der potentiellen Energie bei $T \simeq 1800$ K wurde gefunden, das einer Verdichtung des Materials von 2,17 auf 2,47 gcm^{-3} entspricht; die Volumenabnahme beträgt ungefähr 12%. Die folgenden Aktivierungsenergien für die atomare Diffusion wurden berechnet: 3,43 eV für Si, 3,63 eV für C und 2,94 eV für N. Nach diesen Rechnungen besitzen Kohlenstoffatome die höchste Aktivierungsenergie, was bedeutet, dass

sie die langsamste Atomart im Netzwerk darstellen. Phasenseparation erfolgt deshalb vor allem aufgrund der Si- und besonders der N-Beweglichkeit.

Bevor versucht wurde, Kristallwachstum zu simulieren, war es notwendig zu zeigen, dass empirische Potenziale die Kristallisationsvorgänge in komplexen kovalenten Verbunden beschreiben können. Eine vorläufige Untersuchung des Kristallisationsvorganges in Kohlenstoff lieferte unerwartete Ergebnisse. Kristallwachstum eines Diamantkeimes wurde simuliert durch Temperaturbehandlung einer kubischen Zelle von amorphem bzw. kristallinem Kohlenstoff (Diamant), die eine kristallin/amorph-Grenzfläche enthielt. Diamant stellte dabei den Kristallisationskeim dar. Kristallwachstum erfolgte mit verschiedenen Wachstumsraten, die von der Anlasstemperatur abhängig waren. Eine mittlere Aktivierungsenergie für das Kristallwachstum von $\simeq 2,9$ eV wurde berechnet. Anschließend wurde die Auswirkung einer Korngrenze im Diamantkeim untersucht. Das Wachstum der Grenzfläche und die Bildung von Defekten wurden dabei beobachtet. Schließlich wurde das größte Flächen/Volumen-Verhältnis berechnet, das der Keim besitzen muss um Kristallisation einzuleiten.

Diese Ergebnisse zeigen, zusammen mit den Literaturdaten der Siliziumkristallisation, dass MD-Simulationen in der Lage sind, die Kristallisation dieser beiden einkomponentigen kovalenten Systeme (Silizium und Kohlenstoff) mit kubischer Symmetrie zu modellieren.

Die Kristallisation von kubischem SiC aus dem amorphen Zustand wurde dann durch die Temperaturbehandlung einer kubischen Zelle von amorphem und β -SiC, die durch eine kristallin/amorph-Grenzfläche getrennt sind, studiert. β -SiC dient dabei als Kristallisationskeim. Die Abhängigkeit des Wachstumsprozesses von der kristallographischen Orientierung der kristallin/amorph-Grenzfläche wurde durch Betrachtung von drei verschiedenen Kristallebenen als Grenzfläche, der $\{100\}$ -, $\{110\}$ - und $\{111\}$ -Ebenen, untersucht. Im betrachteten Druck-Temperatur-Bereich wurde für die $\{110\}$ -Ebenen, die $\{111\}$ -Ebenen mit Einfachbindungen und die $\{111\}$ -Ebenen mit Dreifachbindungen Kristallisation beobachtet. Es wurde festgestellt, dass die $\langle 110 \rangle$ -Richtungen die bevorzugten Wachstumsrichtungen sind. Daraus wurde

aber gefunden, dass das Wachstum abbricht oder sich um Größenordnungen verlangsamt, wenn sich $\{111\}$ -Siliziumlagen bilden, die dreifach mit dem Kristall gebunden sind. Es wurde geschlossen, dass das Wachstum durch Facettierung parallel zu den $\{111\}$ -Kristallebenen erfolgt und dass Si-terminierte Flächen vorherrschend sind. Dies steht in guter Übereinstimmung mit experimentellen Daten.

Zusammenfassend kann man feststellen: In der vorliegenden Arbeit wurde der Übergang von der amorphen Si-C-N-Keramik zu einem polykristallinen Material untersucht, indem die grundlegenden Schritte einzeln betrachtet wurden. Zuerst wurde die Phasenseparation untersucht, indem die Abhängigkeit der atomaren Struktur von der chemischen Zusammensetzung von Si-C-N betrachtet wurde. Dabei wurde insbesondere die Bildung monoatomarer graphitischer Lagen beobachtet. Die Simulation der thermischen Entwicklung von Si-C-N erlaubte dann, die Volumenabnahme und die atomare Diffusion zu beobachten und zu quantifizieren. Schließlich wurden die mikroskopischen Mechanismen untersucht, die beim Kristallwachstum von β -SiC aus dem amorphen Zustand auftreten. Es wurde gefunden, dass das Kristallwachstum entlang bevorzugter Kristallebenen erfolgt und dass Si-terminierte Oberflächen gebildet werden.

Die Ergebnisse dieser Arbeit stehen in guter Übereinstimmung mit experimentellen Daten. Darüber hinaus sagen sie das Verhalten der betrachteten Materialien unter Bedingungen voraus, die experimentell nicht zugänglich sind; auf diese Weise können allgemeine Schlußfolgerungen gezogen werden.

Dies Arbeit eröffnet daher neue Perspektiven für das Studium kovalenter Keramiken mit MD-Simulationen. So sind z. B. die Auswirkung äußerer Spannungen auf das Gefüge der amorphen und polykristallinen Si-C-N-Materialien sowie die atomaren Prozesse, die die Oxidation begleiten, wichtige offene Fragen. In der Tat müssen keramische Materialien, die für Anwendungen bei hoher Temperatur verwendet werden, ausgezeichnete Eigenschaften bezüglich Oxidationsbeständigkeit, Kriechverhalten und Bruchfestigkeit haben

Außerdem wurde kürzlich entdeckt, dass aus Prekursor-Polymeren hergestellte Si-C-N-Keramiken, die Bor enthalten, eine höhere thermische Stabilität besitzen können als ternäre Si-C-N-Keramiken. Das Gefüge des amorphen Si-B-C-N-Materials sowie die atomaren Mechanismen, die bei der Kristallisation und der mechanischen Belastung beteiligt sind, sind nicht vollständig bekannt. Erste Simulationen von Si-B-C-N-Systemen wurden mit dem Ziel durchgeführt, die Zuverlässigkeit des Wechselwirkungspotenzials zu prüfen, wenn im Si-C-N-System Boratome enthalten sind.

Ein entscheidender Punkt bei der Phasenseparation, der zur Zersetzung des amorphen Materials führt, ist die Diffusion von Atomen im amorphen Netzwerk. Eine weitere interessante Erweiterung sind deshalb das Auffinden einer Methode zur Berechnung des "Freien Volumens" in Si-C-N- und Si-B-C-N-Materialien und die Untersuchung seines Einflusses auf die atomare Diffusion und auf die mechanischen Eigenschaften dieser Materialien.

Introduction

Silicon carbon nitride Si-C-N ceramics are covalent non-oxide ceramics which possess unique high thermal, chemical, and mechanical stability making them suitable candidates for high temperature applications [1]. A preparation method of these covalent ceramics is the thermal degradation of precursor organic polymers [2, 3, 4]. This process results in oxide-free amorphous Si-C-N ceramics very homogeneous down to the atomic level. Moreover, the microstructure can be, up to a certain level, designed by choosing the appropriate polymer precursors [5, 6, 7]. The final composition $\text{Si}_a\text{C}_b\text{N}_c$ of the ceramic products depend on the particular polymer structure and generally falls within the limits of the three-phase region C-SiC-Si₃N₄ in the phase diagram of the Si-C-N system [8, 9]. The amorphous character of these materials has been demonstrated by X-ray diffraction and microscopic analysis [10, 11, 12].

Si-C-N ceramics remain in their amorphous metastable state up to high temperatures around 1800 K. However, when these materials are annealed at higher temperatures many desirable properties of the amorphous ceramic are eventually lost. In fact, the amorphous material undergoes a transition into the thermodynamically stable crystalline phases, namely graphite, α -Si₃N₄, β -SiC, and gaseous N₂. The interconnecting amorphous network is therefore destroyed. This transition is accompanied by shrinking and cracking of the Si-C-N materials.

The crystallization behavior of these polymer-derived ceramics is believed to consist in a stepwise change of the microstructure, initiated by the rearrangement of the polymer network structure during heat treatment, which leads to phase separation into carbon-rich, silicon/nitrogen-rich, and silicon/carbon-rich amorphous domains. The change in local chemistry and the formation of the gas phase (escape of molecular nitrogen, N₂) support outer and inner crystallization of the relative phases, graphite, silicon nitride (α -Si₃N₄), and cubic silicon carbide (β -SiC) [9, 11, 12, 13]. However, the crystallization temperature of the ceramics exceeds considerably the crystallization temperatures of amorphous SiC (\simeq 1270 K [14]) and of amorphous Si₃N₄ (\simeq 1470 K [15]). To explain this peculiarity, recent results [16, 17] have pointed out that

the silicon/nitrogen and the silicon/carbon phases could coexist in a single amorphous phase, named am-*SiCN*. The carbon-rich phase would stand apart and is often referred to as "free carbon" phase [18, 19].

The structure of the am-*SiCN* phase and its structural modification during annealing have been extensively investigated by means of nuclear magnetic resonance, high resolution electron microscopy, and by neutron and electron diffraction [9, 10, 11, 12, 18, 20, 21, 22]. Despite these studies, the atomic structure of the amorphous, as well as the complete mechanism of the phase transformation leading to crystallization and degradation of the ceramics, are still not completely known.

The aim of our work has been to shed light on the atomistic scale of these materials structures and on the microscopic mechanisms involved in their degradation.

Si-C-N materials are numerically modeled by classical molecular dynamics (MD) methods where the atomic interactions are modeled according to newtonian physics laws. In fact, the time and length scales of the phenomena we want to study go beyond the possibilities of ab initio calculations where quantum mechanical effects are taken explicitly into account. The choice of classical MD is therefore problem driven. This implies the use of empirical potentials to model the atomic interactions. For strongly covalent materials like Si-C-N the best available empirical potential is the one developed by J. Tersoff [23, 24].

The simulations are divided in two major parts, one dealing with the simulation of amorphous Si-C-N structures and the other dealing with crystal growth. In the first part, we simulate the atomic structure of Si-C-N homogeneous materials with different compositions and then follow the thermal evolution of one particular system, experimentally very well characterized, named VT50 [10, 21]. In the second part, after preliminary simulations on diamond crystal growth, we simulate the crystal growth of cubic SiC from the amorphous phase at high pressure.

Besides the crystallization process of the amorphous Si-C-N ceramics, the crystallization of cubic SiC from the amorphous material is a problem of general scientific interest. In fact, among the different SiC polytypes, crystalline cubic SiC is a widely applied ceramic, having high values of electron mobilities, critical electric field, and thermal conductivity.

Parts of the original calculations upon which this thesis is based, have been published in Refs. [25] and [26].

This thesis is organized as follows. In Chapter 2 we give a literature survey on precursor-derived ceramics. In Chapter 3 we describe the modeling of the ceramics by classical molecular dynamics. In Chapters 4 and 5 we report the results of the simulations. Finally, in Chapter 6 conclusions and perspectives are outlined.

Precursor-Derived Si-C-N Ceramics

Structural ceramics for high temperature applications should embody the following properties: oxidation resistance, chemical stability, resistance to creep cavitation at interfaces, sufficient toughness at ambient temperature, and thermal shock resistance [1].

Silicon carbonitride ceramics (Si-C-N) are covalent non-oxide ceramics with unique properties like high strength and toughness [27], high chemical and thermal stability [9, 28], as well as good oxidation [29, 30, 31] and creep resistance [32, 33, 34, 35, 36], combined with low density. These properties are exhibited over a wide temperature range, making them suitable candidates for high temperature applications such as structural parts for motor engines, gas turbines, catalytic heat exchangers and combustion systems.

Conventionally, amorphous Si-C-N ceramics are synthesized through powder sintering. Due to the low self-diffusion of covalently bonded atoms, sintering aids like yttria, alumina or magnesia have to be added for the densification process. These sintering aids are of oxide type and therefore degrade the above mentioned unique properties of the ceramics. Since Verbeek and Winter [2] and Yajima *et al.* [3] succeeded in the mid 1970s in obtaining Si-C-N and SiC fibers from organo-silicon polymers, it is now well established that these ceramics can also be produced by pyrolysis (thermal treatment) of appropriate polymeric pre-ceramic compounds, yielding silicon-based non-oxide ceramics [4]. This preparation method allows the fabrication of materials with high purity and atomic homogeneity because the elements that compose the final ceramic are already bonded to each other on the atomic level within the starting precursor. Moreover it provides a means for controlling and designing the microstructure of ceramic materials in a totally innovative and successful way [5, 6, 7, 37].

The pyrolysis of organo-silicon polymers promotes the organic–inorganic transition at low temperatures $\simeq 1100 - 1400$ K, giving an amorphous material. The “as pyrolyzed” ceramics have very low atomic mobilities and thus remain amorphous up to rather high temperatures $\simeq 1800$ K. Further heat treatment at higher temperatures promotes crystallization

into the thermodynamically stable phases. This results in a partially or entirely crystallized material. Crystallization depends strongly on the chemical composition and microstructure of the materials and on the atmosphere applied. Under certain conditions, crystallization can be delayed up to 1800°C, like in Si-B-C-N ceramics where boron atoms are included in the Si-C-N network [38, 39, 40, 41, 42]. However, crystalline materials, too, are of great interest since their microstructure can be controlled during the process. This can provide a way of stabilizing the desired nano-sized crystal morphologies [29].

To exploit the full potential of polymer ceramics, comprehensive knowledge of the effect of polymer architecture on the ceramization mechanism, and on the final microstructure after amorphous/crystalline transformation is required.

In this chapter we first describe the synthetic path to precursor-derived Si-C-N ceramics, then we resume the observations and calculations meant to understand the crystallization processes, and finally we describe some technical applications.

2.1 Preparation of the Amorphous Ceramic

The complete process for the formation of precursor-derived amorphous ceramics is outlined in Fig. 2.1. It consists in three major steps. One further step is responsible for the crystallization of the ceramic.

- Synthesis of precursor polymers starting from suitable organo-silicon monomers.
- Cross-linking of precursors to give three dimensional pre-ceramic networks.
- Pyrolysis (thermal treatment) of pre-ceramic networks that are transformed into inorganic amorphous materials (organic/inorganic transition). Pyrolysis temperatures usually range from $\simeq 1100$ to $\simeq 1400$ K.

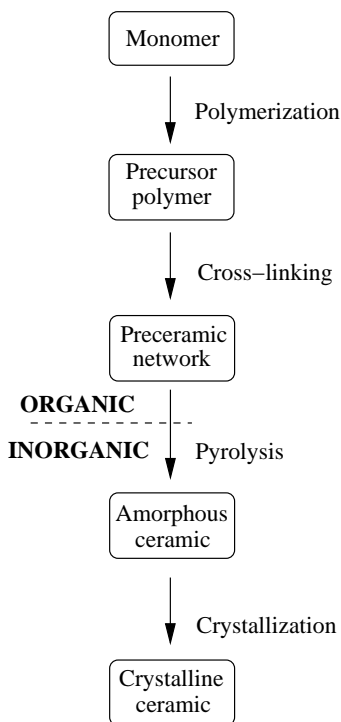


Figure 2.1: *Synthetic path to precursor-derived ceramics.*

- Crystallization of the amorphous solid into thermodynamically stable phases via different metastable intermediates.

The general idea behind the ceramization process is to generate preferred structural features in the organo-silicon precursor network and to subsequently transform the precursors into ceramics under retention of the specially designed building blocks. Pyrolysis must thereby include a series of controllable condensation steps to give the specific architecture of the desired ceramic material.

The pyrolysis of polymer precursors is a rather complex process that involves many chemical reactions in the solid state as well as in the gas

phase. This process has been studied extensively for different precursors polymers by many researchers, among which J. Bill, F. Aldinger, and coworkers [8, 10, 20, 43]. It has been found that the breaking of covalent bonds during the precursor-ceramic conversion is accompanied by the loss of carbon-, hydrogen-, and nitrogen-containing gaseous species, leaving pores in the material and giving rise to density changes. However, owing to the open porosity, the gaseous reaction products of the conversion can be removed without the formation of cracks. The physical nature of the porosity can be classified in three ways. The first two types can be addressed as open porosity and closed porosity. The open pores, which are initially accessible by an external fluid (or gas), change their topology to pinch off into pores which are totally enclosed within the matrix (close porosity), as the material densifies [44]. Generally, such pores are much larger than the molecular dimension. The residual open porosity is of the order of 10% [4, 45] for bulk ceramics. The third type of porosity gives rise to nanoporosity in the material, is determined by its molecular structure and it is usually referred to as "free volume".

The difficulties in making dense bulk materials limits the Si-C-N ceramics applications for low dimensionality-systems, such as thin films, fibers, etc. Moreover, near net shape manufacturing of polymer-derived ceramics is difficult to perform and requires either passive or reactive filler materials to inhibit the shape distortion.

Different types of polymers can be used for the cross-linking and subsequent ceramization. The two organo-silicon polymer precursors of Si-C-N ceramics are carbon-containing polysilazanes and polysilylcarbodiimides. We will not discuss in detail the polymer synthesis from the monomers, an exhaustive review has been recently written by Weinmann and Aldinger [7]. Starting from different polymers precursors yields to ceramics having different chemical compositions and therefore different atomic structures leading to different mechanical and thermal properties. The ternary composition diagram in Fig. 2.2 shows three types of Si-C-N ceramics. Precursor polysilylcarbodiimides, rich in nitrogen, usually give ceramics with compositions located on the tie-line C-Si₃N₄ (a), while ceramics derived from polysilazanes with the general structure [(R¹)(R²)Si-NH]_n (R¹, R² = single-bonded organic units) are located in the three-phase field SiC-Si₃N₄-C (b). Compositions lo-

cated in the three-phase field SiC-Si₃N₄-Si (c) were recently obtained by co-pyrolysis of polycarbosilane and perhydridopolysilazane [12].

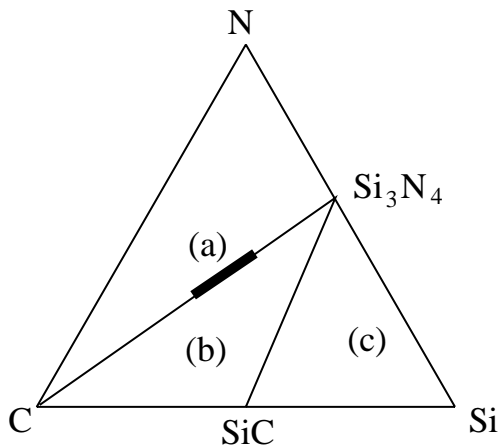


Figure 2.2: Ternary Si-C-N composition diagram. (a) compositions on the tie-line C-Si₃N₄; (b) compositions in the three-phase field SiC-Si₃N₄-C; (c) Compositions located in the three-phase field SiC-Si₃N₄-Si.

2.2 High temperature behavior

Due to the low self-diffusion of the atomic species, precursor-derived Si-C-N ceramics are kinetically stable in their amorphous state at high temperatures. However, solid amorphous materials are in a non-equilibrium state and therefore tend towards crystallization. The crystallization process is started from a phase separation into different amorphous domains. In fact, spectroscopic methods such as solid-state magic angle spinning nuclear magnetic resonance (MAS-NMR), Raman spectroscopy, electron spin resonance (ESR), high resolution transmission electron microscopy (HRTEM) and infrared (IR) spectroscopy in combination with X-ray diffraction (XRD) and wide- and

small-angle neutron scattering, reveal a partial segregation of the amorphous ceramic into structural units that refer to the thermodynamically stable phases. In other words, a phase separation of amorphous silicon/nitrogen-rich, silicon/carbon-rich, and/or carbon-rich domains is observed [9, 11, 12, 13, 16, 18, 19, 28, 46]. This phase separation depends on the chemical composition of the precursors as well as on their atomic structure. At higher temperature the amorphous domains transform into crystalline α -Si₃N₄, β -SiC, and eventually graphitic C. This transformation is accompanied by escape of gaseous N₂, leading to crack formation. Further heat treatment leads the polycrystalline ceramic to decomposition. A complete understanding of the process and of the single steps involved in it is still missing.

In order to get some theoretical understanding of the underlying thermodynamics of the phenomena, Seifert and coworkers [28] have calculated the phase equilibria and made thermal analysis of the Si-C-N ceramics. From their work, it turned out that the decomposition at high T of these ceramics is mainly controlled by the following reactions:



These decomposition reactions depend strongly on the nitrogen partial pressure. Increasing this pressure to 10 bar, for example, results in a shift of the decomposition temperature to $\simeq 2000$ K for the first reaction, in presence of "free" C. As mentioned above, the chemical composition influences the high temperature properties. Here, we discuss briefly the decomposition behavior of two different Si-C-N ceramics, namely *VT50* and *NCP200* [10, 20, 21], having different compositions. The first has stoichiometry Si₂₄C₄₃N₃₃ and has been obtained by pyrolysis of commercially available poly(vinylsilazane), while the second has stoichiometry Si₃₇C₃₂N₃₁ and has been obtained by pyrolysis of polyperhydridosilazane. The calculated phase diagram obtained by Seifert and coworkers [28] is reproduced in Fig. 2.3. The (a) diagram represents phase equilibria for 1687 K < T < 1757 K. In this temperature range three 3-phase regions are stable: 1) C-Si₃N₄-N₂(gas), 2) C-Si₃N₄-SiC, and 3) Si₃N₄-SiC-Si(liquid). Below 1687 K (melting point of silicon), the last phase is composed of solid Si. The composition of *VT50* is located in

the tie-line $\text{Si}_3\text{N}_4\text{-C}$. Assuming quantitative segregation into the pure stable phases, the sample will be, after crystallization, composed of silicon nitride ($\alpha\text{-Si}_3\text{N}_4$) and graphite. The composition of the *NCP200* material is located within the 3-phase region $\text{C-Si}_3\text{N}_4\text{-SiC}$. Accordingly, a fully crystalline material would be made of graphite, cubic silicon carbide ($\beta\text{-SiC}$), and silicon nitride crystallites. The calculations predict that raising the temperature to above 1757 K (Fig. 2.3(b)), leads to the thermal carbo-reduction of Si_3N_4 , according to the above mentioned decomposition reaction. The expected quantitative loss of nitrogen in the case of *VT50* ceramic should result in the formation of a SiC/C composite, while *NCP200* should give a composition located on the $\text{Si}_3\text{N}_4\text{-SiC}$ tie-line. The calculations have been confirmed by X-ray diffraction experiments of annealed ceramic samples. For temperature above 2114 K Si_3N_4 decomposes into single elements, liquid Si and gaseous N_2 .

2.3 Applications

The wide variety of available organo-silicon polymers offers exceptional opportunities for the development of PDCs. In fact, bulk ceramics, fibers, coatings, fiber matrix composites and near-net shape components are achieved.

Bulk ceramics can be obtained by polymer powder compaction, usually achieved by cold, warm, or hot isostatic or uniaxial pressing (depending on the physical/chemical properties of the precursor) and subsequent ceramization. The polymer powder compaction process for the preparation of PDC bulk objects by cold isostatic pressing (CIP) was developed by Riedel *et al.* [4, 47].

The absence of low-melting grain boundary phases in precursor-derived materials leads to extraordinary high temperature mechanical properties that can be very different from those of sintered ceramics. Christ *et al.* [40] as well as Thurn *et al.* [34] observed that the temperature dependence of the creep behavior of Si-C-N ceramics is comparably low and qualitatively the same for all temperatures.

PDC coatings can protect sensitive substrates from hydrolysis, oxidation, corrosion, and erosion. In contrast to chemical and physical vapor

deposition, which are expensive procedures for obtaining ceramic coatings, the formation of ceramic coatings by a dip-coating process is a rather simple and comparably economic process. The substrate is introduced into a solution of the polymer precursor, pulled out, dried, and subsequently thermolyzed. The thickness of the adherent polymer layer can be varied by changing parameters such as pull-out velocity, solution viscosity, polymer concentration, and the number of the coating-thermolysis cycles. High velocity, viscosity, and polymer concentration result in an increase of the polymer (and thus ceramic) layers in thickness and vice versa. Unfortunately, with increasing thickness, coatings tend to crack during pyrolysis. This is mainly a consequence of the loss of gaseous by-products during the heat treatment and an increase in density during the polymer-to-ceramic transformation.

A multifaceted field, which is currently under investigation, is the protection of carbon-fiber-reinforced ceramic composites from oxidation, hydrolysis, and erosion by PDC coatings. Because of their high maximum application temperature and low density, carbon-fiber-reinforced composites are very promising materials for realizing mechanical chargeable, light-weight structures with a high potential for aerospace applications.

The fabrication of high-modulus refractory ceramic fibers requires controllable polymer rheology and adjustable polymer reactivity. Precursor fibers are obtained by either melt or dry spinning. Different principles for fiber processes such as extrusion, down drawing from preforms, or up drawing from precursor melt or solutions are known. Once spun the precursor fiber is rendered infusible by subsequent curing, which represents an additional chemical surface reaction. Without this step, fiber integrity is lost because of melting and/or creep of the green fiber before full transformation into the ceramic state.

Even though many Si-C-N precursors have been published since the mid-1970s, there are only very few procedures described in the literature dealing with the conversion of such polymers into ceramic fibers.

Fiber-reinforced ceramic matrix composites (CMCs) have been shown to exhibit extraordinary thermo-mechanical properties combined with low density. They are consequently highly interesting candidates for many-fold applications under severe conditions, especially in aerospace. CMCs

can be obtained by different methods. The most established procedures are liquid-phase routes, gas-phase routes, or their combination.

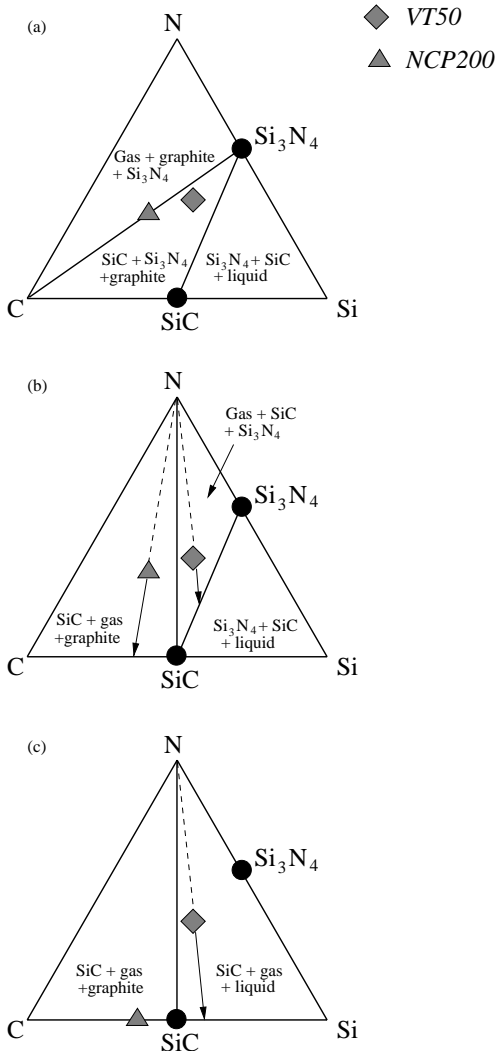


Figure 2.3: Ternary Si-C-N phase diagrams including compositions of ceramics VT50 (triangles) and NCP200 (rhombs) at $P=1 \text{ atm N}_2$ at different temperatures: (a) $1687 \text{ K} < T < 1757 \text{ K}$; (b) $1757 \text{ K} < T < 2114 \text{ K}$; (c) $T > 2114 \text{ K}$. Decomposition of as-pyrolized VT50 ceramics above 2114 K occurs in one step delivering SiC/C composites, whereas decomposition of NCP200 ceramic proceeds in two steps [10, 28].

Modeling of Covalent Ceramics by Molecular Dynamics

Materials are made of interacting atoms and their physical and chemical behavior is governed by the laws of electromagnetism and of quantum mechanics. Going one step further, a system of interacting atoms is an assembly of nuclei and electrons. With the exception of very light atoms (H, He) the nuclear motion obeys to a very good approximation, in most circumstances, the laws of classical mechanics. In any state of aggregation (gaseous, solid, liquid) the nuclei are subject to thermal motion.

When the system is in thermal equilibrium, the nuclear kinetic energy fluctuates around the average value dictated by the equipartition theorem at the given temperature. Molecular dynamics (MD) is a technique for computing the equilibrium properties of a classical many-body system, once the interactions are known.

The motion of N classical particles is governed by Newton's equation:

$$-\frac{dV(\mathbf{R})}{d\mathbf{R}} = m\frac{d^2\mathbf{R}}{dt^2} \quad (3.1)$$

$$\mathbf{R} \equiv (\mathbf{r}_1, \mathbf{r}_2, \dots, \mathbf{r}_N) \quad (3.2)$$

where $V(\mathbf{R})$ is the potential energy, and \mathbf{R} is the set of all Cartesian coordinates of their centres of masses, i.e. a vector in a $3N$ -dimensional space. \mathbf{F} is the force acting on the particles, and \mathbf{a} is the acceleration vector. This is a set of $3N$ coupled linear differential equations, which we integrate numerically for a certain interval of time Δt , as explained in appendix A.

In this work we have used the IMD (ITAP Molecular Dynamics) code, developed at the Institut für Theoretische und Angewandte Physik [48, 49, 50].

The crucial ingredient in MD simulations in order to simulate a multi atomic system is, besides nuclear masses, the potential energy $V(\mathbf{R})$ summarizing the interatomic interactions. The term “force field” is

sometimes used as a synonym. This force field, which holds the system together, is of electronic nature: therefore its behavior is very far from the classical limit, and would require solving the many-electron Schrödinger equation while the system evolves in time. Nowadays, this is indeed possible (so-called *ab-initio* MD), but only when sizes N and times t are smaller, by several orders of magnitude, than those envisaged in the present research and dictated by the nature of the materials we are addressing. It is therefore mandatory, as in most MD simulations, to rely on a classical force field which models the interatomic interactions. The mathematical formulation of the potential depends on the chemical and physical nature of the system studied. For covalent materials, a successful model has been proposed by J. Tersoff some years ago [23, 24, 51, 52, 53].

No matter how large the simulated system is, its number of atoms N is negligible compared with the number of atoms contained in a real macroscopic system (order of 10^{23}), and the ratio between the number of surface atoms and the total number of atoms would be much larger than in reality, causing surface effects to be much more important than what they should. A solution to this problem is to use periodic boundary conditions (PBC). When using PBC particles are enclosed in a box, and we can imagine this box replicated to infinity by translation in all three Cartesian directions. All the “image” particles move together, and only one of them is represented in the computer as shown schematically in Fig. 3.1.

3.1 Thermodynamic and structural properties

MD is a deterministic technique: given an initial set of positions and velocities, the subsequent time evolution is in principle completely determined. The computer generates a series of time-correlated points, a *trajectory*, in a $6N$ -dimensional phase space whose coordinates are the three Cartesian components of position vectors \mathbf{r}_i and momentum vectors \mathbf{p}_i . However, such trajectory is usually not particularly relevant by

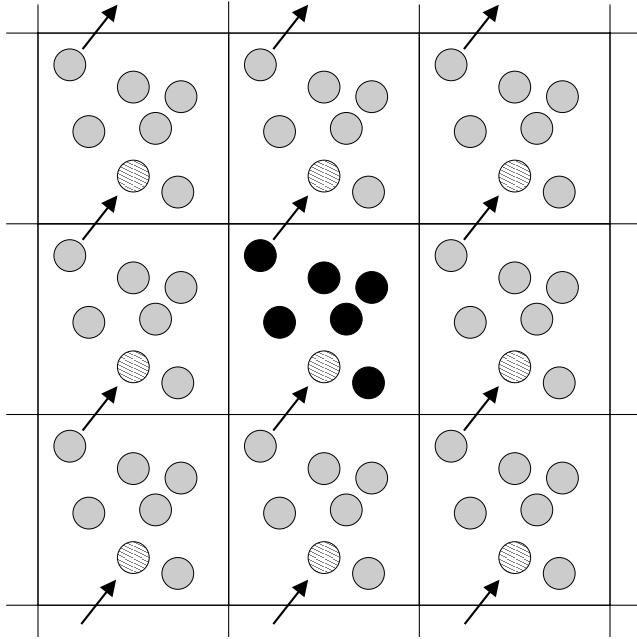


Figure 3.1: *Periodic boundary conditions, a two dimensional system. Particles can enter and leave each box across each of the four edges. In a three-dimensional example, particles would be free to cross any of the six cube faces. Particles interact with real and image particles which are within the potential cut-off distance.*

itself. The link between calculated trajectories and macroscopic observable is statistical mechanics.

According to statistical mechanics, macroscopic observables can be calculated as averages over all configurations distributed according to the Boltzmann probability function. If a representative collection of configurations can be generated then the sum over all states can be approximated by an average over a finite set of configurations. Representative here means that the number of configurations with a given energy is proportional to that given by the Boltzmann distribution, and that all

“important” parts of the phase space are sampled. We can denote such points in phase space by their positions and momenta, where M is the number of points.

$$\langle X \rangle_M = \frac{1}{M} \sum_i^M X(\mathbf{r}_i, \mathbf{p}_i) \quad (3.3)$$

A collection of configurations is called an *ensemble*. $\langle X \rangle_M$, the macroscopic calculated observable, is an ensemble average. If the configurations are generated by following the time evolution of the system, as in MD methods, the average is formally a time average. By the ergodic hypothesis this is assumed to give the same as an average over an ensemble.

$$\langle X \rangle = \lim_{\tau \rightarrow \infty} \frac{1}{\tau} \int_0^\tau X(t) dt = \lim_{M \rightarrow \infty} \frac{1}{M} \sum_i^M X_i \quad (3.4)$$

A trajectory obtained by MD provides the desired set of configurations. Therefore, a measurement of a physical quantity by simulation is simply obtained as an arithmetic average of the various instantaneous values assumed by that quantity during the MD run. In order to obtain an acceptable statistical error, the averaging is typically performed on $10^3 - 10^5$ points in phase space.

3.1.1 Temperature and pressure

The temperature is related to the average kinetic energy and can be calculated with the help of the equipartition theorem:

$$\frac{1}{2}(3N - N_C)k_B T = \frac{1}{2} \left\langle \sum_i^N m_i \mathbf{v}_i^2 \right\rangle_M \quad (3.5)$$

Where $(3N - N_C)$ is the number of degrees of freedom, equal to three times the number of particles minus the number of constraints N_C .

The pressure can be calculated by making use of the virial theorem. The *virial*

$$W = \frac{1}{3} \sum_{i < j}^N \mathbf{r}_{ij} \cdot \mathbf{f}_{ij} \quad (3.6)$$

describes the deviation of the equation of state of a van der Waals gas from an ideal gas due to the interactions between the atoms. \mathbf{r}_{ij} is the distance vector between the i -th and the j -th atom, \mathbf{f}_{ij} is the interaction force between them. In order to obtain the total pressure P , the average virial value has to be added to the equation of state of the ideal-gas:

$$PV = Nk_B T + \langle W \rangle_M \quad (3.7)$$

An ensemble may be characterized by parameters which are fixed, and those which can be derived from the simulation data. Ensembles generated by MD methods are naturally of the NVE type (constant number of particles, constant volume and constant potential energy). This method can be modified to simulate other ensembles like the NVT (constant volume and temperature) or the NPT (constant pressure and temperature). The NPT ensemble is of special importance because it relates directly to most experimental conditions. Details of these techniques can be found in Ref. [54]. The MD calculations in this work were performed in the NVT and in the NPT ensembles.

3.1.2 Distribution functions

Distribution functions measure the average value of a property as a function of an independent variable. A typical example is the radial distribution function $g(r)$ which measures the probability of finding a particle as a function of distance from a ‘typical’ particle, relative to that expected from a completely uniform distribution (i. e. an ideal gas with density N/V). The radial distribution function is defined as

$$g(r) = \lim_{\Delta r \rightarrow 0} g(r, \Delta r) \quad (3.8)$$

$$g(r, \Delta r) = \frac{V}{N^2} \frac{\langle N(r, \Delta r) \rangle_M}{2\pi r^2 \Delta r} \quad (3.9)$$

where $N(r, \Delta r)$ is the number of particles between r and $r + \Delta r$ from another particle, and $4\pi r^2 \Delta r$ is the volume of a spherical shell with thickness Δr . By construction, $g(r) = 1$ in an ideal gas. Any deviation of $g(r)$ from unity reflect correlations between the particles due to intermolecular interactions. The position of the first peak gives the mean length of the chemical bond, while the integral area under the peak gives the number of atoms involved in the bond.

For amorphous solid systems and for molecular liquids, the radial distribution function can be extended to the orientational degrees of freedom in order to characterize the angular distribution.

3.2 Modeling covalent materials

Materials are physical systems made of interacting atoms. The atomic interactions type determines the physical and chemical behavior of the materials. The model ability to describe the atomic interactions determines the realism of a simulation. Atomic interactions are modeled by a parametrical function $V(\mathbf{R})$ depending on all the atomic coordinates. In *ab-initio* simulation methods, the atomic interactions are calculated on a quantum mechanical basis. Quantum mechanics is the best, most exact available mathematical description of atomic interactions. However, up to the present days, *ab-initio* methods have severe size and time limitations. Only systems of approximately 100 atoms for a maximum period of time of 10 ps can be afforded on large supercomputers. For larger systems and longer simulations, other simpler, more approximate description models are required.

In ‘classical’ MD simulations atomic interactions are modeled according to classical physics laws and the quantum mechanical effects are totally neglected. In a classical simulation both the size and the time can be chosen greater than the above values by about 2 orders of magnitude. Simulations in the nanometer/nanosecond scales can be afforded. The obvious drawback of these methods is the reduced accuracy of the simulation, which however is not a major problem when qualitative issues are relevant.

The starting point for a classical MD simulation is to choose an analytical function $V(\mathbf{R}) = V(\mathbf{r}_1, \dots, \mathbf{r}_N)$ of the atoms positions, representing the potential energy of the system when atoms are arranged in that specific configuration. Forces are then derived as the gradient of the potential with respect to atomic displacements:

$$\mathbf{F}_i = -\nabla_{\mathbf{r}_i} V(\mathbf{r}_1, \dots, \mathbf{r}_N) \quad (3.10)$$

If we consider a system of N atoms, the potential energy $V(\mathbf{r}_1, \dots, \mathbf{r}_N)$ may be partitioned into terms depending on the coordinates of individual atoms, pairs, triplets etc.:

$$V(\mathbf{r}_1, \dots, \mathbf{r}_N) = \sum_i^N v_1(\mathbf{r}_i) + \sum_i^N \sum_{i>j}^N v_2(\mathbf{r}_i, \mathbf{r}_j) + \sum_i^N \sum_{j>i}^N \sum_{k>j>i}^N v_3(\mathbf{r}_i, \mathbf{r}_j, \mathbf{r}_k) + \dots \quad (3.11)$$

The $\sum_i^N \sum_{i>j}^N$ notation indicates a summation over all distinct pairs i and j without counting any pair twice, the same care must be taken for triplets etc. The first term $v_1(\mathbf{r}_i)$ represents the effect of an external field on the system and can thus be neglected when isolated systems are studied. The remaining terms represent the particle interactions. The second term v_2 is the pair potential and it is the most important. The pair potential depends only on the magnitude of the pair separation $r_{ij} = |\mathbf{r}_i - \mathbf{r}_j|$, so it may be written $v_2(r_{ij})$. In many computer calculations, only this pairwise term is included in the potential energy form and can be hereafter denoted simply by $v(r)$, where we denote r_{ij} by r . The pairwise approximation gives a good description of properties of many materials with rather closed packed structures like, for example, solid and liquid noble gases (Ar, Xe, Cr). The average three-body effects can be partially included by defining an ‘effective’ pair potential. The simpler effective pair potentials commonly used in computer simulations reflect the salient features of real interactions in a general, often empirical, way. For example, the Lennard-Jones 12-6 (LJ) potential

$$v^{\text{LJ}}(r) = 4\varepsilon((\sigma/r)^{12} - (\sigma/r)^6) \quad (3.12)$$

provides a reasonable description of the properties of argon, via computer simulation, if the parameters ε and σ are chosen appropriately.

The LJ potential has a long-range attractive tail of the form $-1/r^6$, a negative well of depth ε , and a steeply rising repulsive wall at distances less than $r \sim \sigma$.

Other examples of pair potentials are the Morse potential, the Buckingham potential etc. In Morse-like potentials, like that of Biswas and Hamann [55], the $v(r)$ effective pair potential has the form of $e^{-\alpha r}$. In this case a cut-off function is added to limit the range of the interactions in order to permit a reduction of the computational time.

The two-body approximation present in pair potentials is however very poor for many relevant systems with a more open structure like, for example, semiconductors, ceramics, and all materials that exhibit covalent atomic interactions. Indeed, no reasonable pair potential will ever stabilize the diamond structure. For those materials better models for the covalent atomic interactions are represented by other potentials like the Tersoff potential [23, 51, 52, 53, 24], the Stillinger-Weber potential [56], the Keating [57] potential, and others. In these models atoms are considered spherical and chemically inert.

3.2.1 The Tersoff Potential

The Tersoff potential was developed by J. Tersoff to describe covalent systems. The N -body form of potential was abandoned for a totally new, more empirical, approach. The central idea is that in real systems, the strength of chemical bonds depend on the local environment, i. e. an atom with many neighbors forms weaker bonds than an atom with few neighbors. J. Tersoff developed a pair potential whose strength depends on the environment. It was calibrated first for silicon [23, 51, 52], then for carbon [53] and then for multicomponent systems [24], including germanium.

The potential developed by Tersoff is based on the concept of *bond order* and at first sight, it has the appearance of a pair potential. The energy is modeled as a sum of pair-like interactions, where, however, the coefficient of the attractive term in the pair-like potential (which plays the role of a bond order) depends on the local environment, giving a many-body potential.

For a multicomponent system, the energy E , as a function of the atomic coordinates, is taken to be:

$$E = \sum_i E_i = \frac{1}{2} \sum_{i \neq j} V_{ij} \quad (3.13)$$

$$V_{ij} = f_c(r_{ij})[f_R(r_{ij}) + b_{ij}f_A(r_{ij})] \quad (3.14)$$

Here i and j label the atoms of the system and r_{ij} is the length of the ij bond. The pair-like interactions V_{ij} are sum of a repulsive $f_R(r_{ij})$ and an attractive $f_A(r_{ij})$ function multiplied by $f_c(r_{ij})$, an optional cut-off function to restrict the range of the potential. The b_{ij} term is interpreted as representing bonding, it is thus very important and will be described later.

The attractive and repulsive functions have the form of a Morse potential, related to the exponential decay dependence of the electronic density

$$f_R(r_{ij}) = A_{ij} \exp(-\lambda_{ij}r_{ij}) \quad (3.15)$$

$$f_A(r_{ij}) = -B_{ij} \exp(-\mu_{ij}r_{ij}) \quad (3.16)$$

A_{ij} , B_{ij} , λ_{ij} , and μ_{ij} are all positive parameters, with $\lambda_{ij} > \mu_{ij}$.

The main feature of this potential is the presence of the b_{ij} term. All deviations from a simple pair potential are ascribed to the dependence of b_{ij} on the local atomic environment. The b_{ij} is an empirical function which depends parametrically on:

1. the distances r_{ik} between atom i and third neighbors other than j atom, labeled k atoms;
2. the angle θ_{ijk} between atoms i, j and k ;
3. the chemical type of the k atoms.

The exact mathematical formulation of b_{ij} and the complete set of parameters are in Appendix B.

This potential and the parameters were chosen to fit theoretical and experimental data obtained from realistic and hypothetical silicon configurations, namely the cohesive energy of several high symmetry bulk

structures, lattice constant and bulk modulus of silicon in the diamond configuration. Later it has been calibrated for carbon atoms by J. Tersoff in the same manner, constraining the vacancy formation energy in diamond to have at least 4.0 eV (see Ref. [53]). The potential for carbon atoms only was tested by calculating the cohesive energy and structure of diverse carbon geometries, the elastic properties, phonons, polytypes, and defects and migration barriers in diamond and graphite. The results are in good agreement with experiments and with *ab initio* calculations. The most attractive feature of the potential is its ability

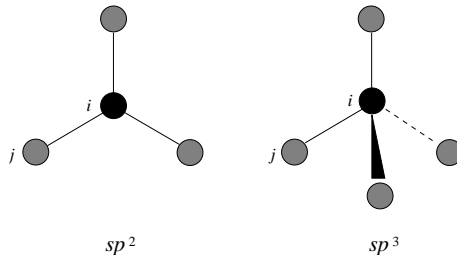


Figure 3.2: Schematic drawing of atoms i with hybridization sp^2 (planar three-fold coordination, left of figure) and with sp^3 hybridization (tetrahedral, four-fold coordination, right of figure).

to describe small energy differences between diamond and graphite, for example. This potential is in fact able to distinguish between different atoms environment, namely between fourfold sp^3 bonds and threefold sp^2 bonds as shown in Figs. 3.2 and 3.3. In Fig. 3.4 the cut-off function for the C-C potential is shown.

The Tersoff potential was also applied to study amorphous carbon formed in three different ways as well as liquid carbon. Results are discussed in Ref. [53]. Other authors [58] applied Tersoff potential to study the transformation of carbon from the bc8 structure to graphite, while others worked on liquid silicon [59]. DeBrito Mota [60] and coworkers worked on amorphous silicon nitride, calculating the parameters for nitrogen.

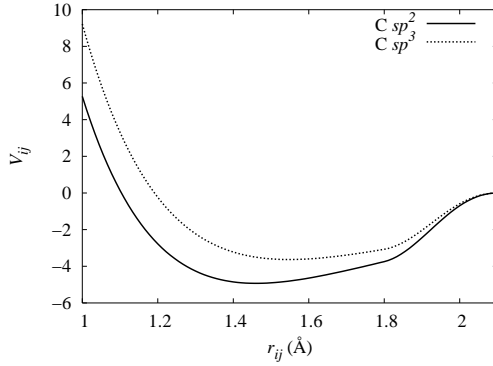


Figure 3.3: Tersoff potential between atom i and j (Fig.3.2) when atom i is in two different hybridizations. Atoms i and j are carbon atoms, parameters are taken from Ref. [53]. The abrupt modification of the potential curve for $r > 1.8\text{\AA}$ is due to the presence of the cut-off function displayed in Fig. 3.4.

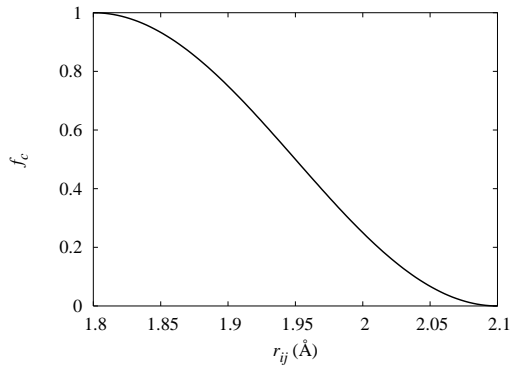


Figure 3.4: Cut-off function for the C-C Tersoff potential [53].

Simulations of amorphous Si-C-N

Before the present study, three theoretical papers [21, 61, 62] have already addressed amorphous precursor-derived Si-C-N ceramics. In the first work, Dürr and coworkers [21] exploited experimental informations from neutron and X-ray scattering data in order to investigate the atomic structure of the amorphous ceramic through a Reverse Monte Carlo calculation. The remaining two papers are MD simulations. The work of Matsunaga *et al.* [61] is based on classical MD simulations with the empirical Tersoff potential, while Amkreutz *et al.* [62] performed *ab initio* MD simulations within a density-functional-based tight-binding scheme. The latter approach, where the atomic forces are calculated on a quantum mechanical basis, is very accurate but has severe size ($\simeq 100$ atoms) and time ($\simeq 1$ ps) limitations.

In this work we perform classical MD simulations of Si-C-N ceramics in the nanometer/nanosecond scales, modeling the atomic interaction by the Tersoff potential [24]. Our work is thus within the same theoretical framework as the one of Ref. [61], but much wider in scope and with improved statistics. In fact, we consider a more various range of compositions, larger samples, and longer, by three orders of magnitude, simulation times. This allow us to achieve a better statistical accuracy. Furthermore, we perform our simulations in the constant number of particles, constant temperature, and constant pressure (NPT) ensemble, whereas in Ref. [61] the simulations are performed in the NVT ensemble (constant volume instead of constant pressure). Working at constant pressure enables us to better reproduce the experimental conditions.

Our results are in good agreement with the previous three theoretical studies as far as the same composition range is considered, and display a rather general behavior for Si-C-N systems.

Very recently two other theoretical studies have been published. In the first [17] a thermodynamic model has been developed to rationalize the enhanced persistence of the amorphous Si-C-N ceramics, while in the second [63] model structures of some polymer-derived ceramics, including amorphous Si-C-N, have been simulated by *ab initio* molecular dynamics. Both works confirm the results of our simulations.

The present chapter is organized as follows: in Section 4.1 we describe how the Tersoff potential has been modified to model Si-C-N amorphous systems. In Section 4.2 we briefly describe the calculation method by which we analyze the atomic configurations. In Section 4.3 we simulate Si-C-N homogeneous amorphous ceramics having different chemical compositions. Finally, in Section 4.4 we follow the thermal evolution of one particular amorphous ceramic, corresponding to the *VT50* experimental sample.

4.1 Modification of the Tersoff Potential

In the simulations described in this chapter we use a modified version of the Tersoff potential described in Section 3.2.1 and Appendix B. In accordance to what has been done by other authors [61, 60], N-N interactions are modified as well as the C-N ones, with the aim of stabilizing the Si-C-N amorphous structures. The attractive parts of the N-N and of the C-N potentials are set to zero, while only the repulsive terms are kept. Concerning the N-N interactions, this modification has been motivated by deBrito *et al.* [60] by the fact that the N-N interactions are extremely strong, producing N₂ molecules with bonding energy of 9.8 eV. Once the N₂ molecules are formed within the amorphous structure, they do not interact with other atoms, diffuse through the system and evaporate through the surface. The modified interaction keeps the N atoms in the amorphous solid, without appreciably affecting other features of the simulations.

Concerning the C-N interactions, Seher *et al.* [64] suggested that C-N bonds in polymer-derived Si-C-N decompose during pyrolysis above $T = 1273$ K and are not observed in the ceramics. For this reason, we prevent the formation of C-N pairs in our simulations.

4.2 Calculation of distribution functions

The main criterion experimentally available for structural characterization of an amorphous material is the radial distribution function (RDF). RDFs are obtained by Fourier transforming the intensity distribution

of X-ray diffraction or neutron scattering experiments. In MD simulations, where the atomic coordinates are known, RDFs are calculated as the average number of atoms at a given distance from another atom as explained in Section 3.1.2 (see equation 3.9).

The RDF of the ternary Si-C-N system is the sum of six partial RDFs, namely the Si-Si, the Si-C, the Si-N, the C-C, the C-N, and the N-N one. As a side product, the RDF allowed us to select an appropriate cut-off in order to define different types of coordination numbers. The total coordination number of an atom of type A is defined as the total number of atoms inside a sphere of a given radius R_{A-B} with center in A, and is referred to as $Z(A)$. The radius of the sphere is $R_{A-B} = 2.2 \text{ \AA}$ for all pair interactions except for the Si-Si pairs where $R_{Si-Si} = 2.9 \text{ \AA}$. Furthermore, it is possible to define the partial coordination number $Z(A)_B$ as the number of atoms of type B which are inside the sphere with center in atom type A and fixed radius.

The bond angle is a parameter very useful in describing the local structure. It is the angle between two bonds originating from the same atom. A “bond” in this context, is the vector joining neighbor atoms. Distribution functions of the bond angles, angular distribution functions (ADFs) can be calculated with the same procedure of RDFs calculations. For the calculation of ADFs we have used the same cut-off of the coordination numbers.

4.3 Dependence of the Atomic Structure on the Chemical Composition

Si-C-N ceramics obtained via pyrolysis of polymers show high homogeneity at the atomic scale level. Their chemical composition can be varied by changing the precursor chemistry, the pyrolysis temperature and atmosphere, and the heat treatment. The polymer synthesis and the cross-linking previous to ceramization are believed to greatly influence the atomic structure of the ceramic. However, although powerful investigation tools such as X-ray diffraction (XRD), solid state NMR, neutron scattering, and transmission electron microscopy (TEM) are available, the microstructure of these ceramics is not yet completely known [8, 9, 11, 20, 21, 28]. In particular, it is not clear whether these materials show phase separation right after their ceramization or not. This is an important issue, because phase separation into amorphous silicon/nitrogen, silicon/carbon, and "free" carbon domains is believed to be the first step toward crystallization of these materials when treated at high temperatures.

In this section we simulate the microstructure of amorphous Si-C-N systems obtained by rapid cooling from the melt. We study the dependence of the atomic structure on the chemical composition.

4.3.1 Method

Five Si-C-N systems, differing in their compositions, are simulated by means of the classical MD method. The simulation box (initial side length $a = 39.1$ Å) contains 4000 atoms and is repeated with periodic boundary conditions. The starting atomic coordinates are obtained by randomly arranging silicon, carbon, and nitrogen atoms on the sites of a face-centered cubic lattice. The systems is then heated and equilibrated at very high temperature in two steps. First at $T \simeq 35000$ K at constant volume for 10 ps, then at $T \simeq 4600$ K at a pressure varying from $P \simeq 90$ GPa to $P \simeq 0$ GPa for another 100 ps.

To prove that the obtained atomic configurations do not depend on the choice of the initial random configuration, several different start configurations have been generated for one specific composition, by choosing

different random seeds. After the heating process the different configurations had the same average atomic structure, allowing us to consider only one configuration for each desired composition.

The stoichiometry of the five Si-C-N systems is $\text{Si}_{24}\text{C}_{43}\text{N}_{33}$ (denoted as *S1* hereafter), $\text{Si}_{48}\text{C}_{40}\text{N}_{12}$ (*S2*), $\text{Si}_{44}\text{C}_8\text{N}_{48}$ (*S3*), $\text{Si}_{12}\text{C}_{40}\text{N}_{48}$ (*S4*), and $\text{Si}_{37}\text{C}_{32}\text{N}_{31}$ (*S5*). The chemical compositions are displayed on the concentration triangle of Fig. 4.1. With this diagram it is possible to see that, for example, *S2* and *S4* have the same C amount, which is very similar also to *S1*. *S3* and *S4*, on the other hand, are equal in their N amount. The two quasi-binary lines C– Si_3N_4 and Si_3N_4 –SiC inside the composition diagram indicate the calculated stable phases [8, 28] between room temperature and $T = 1762$ K. The two systems *S1* and *S5* correspond to the experimental samples investigated in Ref. [10, 21, 20], named *VT50* and *NCP200* respectively. On the Si–N side the quantity η relates to the N/Si ratio. If we draw a line through the C vertices and a Si-C-N system and meet the Si–N side, we know the relative amount of nitrogen and silicon in the systems, regardless of the carbon amount. The five configurations obtained with this procedure are then quenched from $T \simeq 4600$ K to $T = 0$ K with a cooling rate of 2.1×10^9 K/s, for a total of 11×10^6 time steps (corresponding to 2.2 nanoseconds of simulation time). The external pressure is set to zero.

4.3.2 Results of simulations

The calculated total RDFs of the five amorphous systems at $T = 0$ K are shown in Fig. 4.2. The first peak at $r \simeq 1.45$ Å is due to the C-C pairs. The second peak at $r \simeq 1.75$ Å is mostly due to the Si-N pairs. A weak contribution slightly shifting this peak to larger values of r , however, is due to the Si-C pairs ($r \simeq 1.85$ Å). This contribution is larger in the *S2* sample, for reasons which will become clear further down. The third peak at $r \simeq 2.55$ Å is due to the C-C second-neighbor pairs and to a very weak contribution at $r \simeq 2.35$ - 2.45 Å due to the Si-Si pairs. In Table 4.1 we have reported the calculated total and partial coordination numbers for the three atomic species in the five systems. The partial coordination numbers $Z(\text{C})_{\text{N}}$, $Z(\text{N})_{\text{C}}$, and $Z(\text{N})_{\text{N}}$ are solely due to the

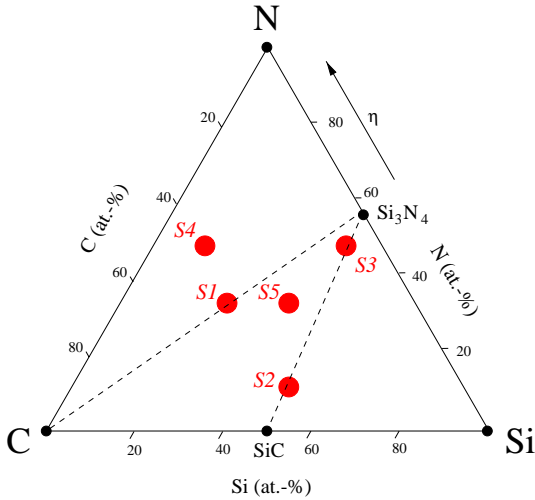


Figure 4.1: Si-C-N concentration diagram, showing the positions of the Si-C-N systems with respect to the quasi-binary lines (dashed) $\text{Si}_3\text{N}_4\text{-C}$ and $\text{Si}_3\text{N}_4\text{-SiC}$.

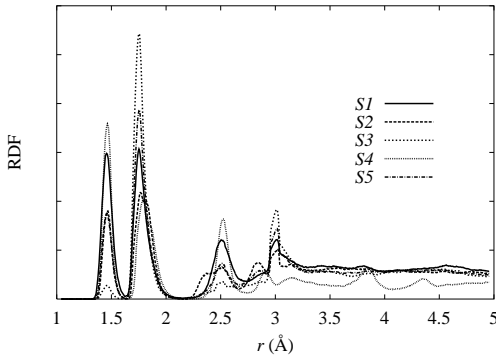


Figure 4.2: Normalized RDF of the five Si-C-N systems quenched to $T = 0$ K.

Table 4.1: Total ($Z(A)$) and partial ($Z(A)_B$) coordination numbers and nitrogen/silicon ratio (η) of the five systems.

Coordination numbers	$S2$	$S5$	$S3$	$S1$	$S4$
$Z(\text{Si})_{\text{Si}}$	2.08	0.99	1.07	0.27	0.00
$Z(\text{Si})_{\text{C}}$	1.32	0.93	0.36	0.64	0.22
$Z(\text{Si})_{\text{N}}$	0.75	2.49	3.26	3.94	7.41
$Z(\text{Si})$ total	4.15	4.41	4.69	4.85	7.63
$Z(\text{C})_{\text{Si}}$	1.59	1.08	2.00	0.36	0.07
$Z(\text{C})_{\text{C}}$	1.53	2.02	1.13	2.73	2.84
$Z(\text{C})_{\text{N}}$	0.01	0.06	0.16	0.05	0.10
$Z(\text{C})$ total	3.13	3.16	3.29	3.14	3.01
$Z(\text{N})_{\text{Si}}$	3.00	2.97	2.99	2.87	1.85
$Z(\text{N})_{\text{C}}$	0.03	0.06	0.03	0.06	0.08
$Z(\text{N})_{\text{N}}$	0.03	0.26	0.43	0.88	3.52
$Z(\text{N})$ total	3.06	3.29	3.45	3.81	5.45
η	0.20	0.46	0.52	0.58	0.80

C-C, C-Si, and Si-N interactions, the N-N and C-N interactions being set to zero.

4.3.2.1 Silicon environment

The silicon total and partial coordination numbers are plotted in Fig. 4.3 as a function of the quantity $\eta = N_{\text{N}}/(N_{\text{Si}}+N_{\text{N}})$, where N_{N} and N_{Si} are the number of nitrogen and silicon atoms respectively. From the plot in Fig. 4.3 we observe the following. First of all, while the partial coordination of nitrogen to silicon, $Z(\text{Si})_{\text{N}}$, increases monotonically with η , the coordinations of silicon and carbon, $Z(\text{Si})_{\text{C}}$ and $Z(\text{Si})_{\text{Si}}$, decrease. The total silicon coordination, $Z(\text{Si})$, also increases monotonically with η . We conclude that silicon atoms are always surrounded by the maximum possible number of nitrogen atoms. However, when $\eta < 0.6$, the $Z(\text{Si})_{\text{N}}$ falls below 4, silicon atoms are surrounded by atomic types other than

nitrogen in order to achieve a total coordination slightly larger than 4, being in the center of mixed tetrahedra $\text{Si}(\text{C},\text{N})_4$. When the nitrogen/silicon ratio is high enough, the nitrogen atoms screen the silicon ones, preventing Si-Si and Si-C interactions. Only this ratio determines whether silicon atoms are tetrahedrally or higher coordinated.

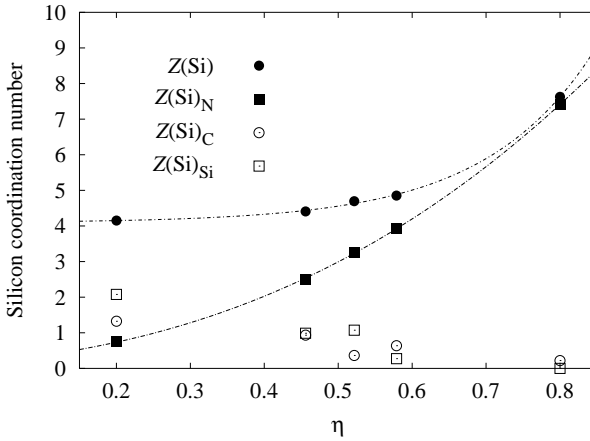


Figure 4.3: Silicon coordination as a function of $\eta = N_{\text{N}}/(N_{\text{Si}} + N_{\text{N}})$. The total silicon coordination number $Z(\text{Si})$ and the partial coordination number $Z(\text{Si})_{\text{N}}$ increase monotonically with η , showing that Si atoms are coordinated to the maximum possible number of N atoms.

Fig. 4.4 shows the calculated bond angle distribution functions (ADFs) of silicon. The broad peak around $\vartheta_{\text{Si}} \simeq 109^\circ$ shows that silicon atoms are more or less tetrahedrally coordinated in all systems except in S_4 where they are higher coordinated due to the high nitrogen/silicon ratio.

We now analyze the $\text{Si}(\text{Si},\text{C},\text{N})_4$ structures in detail, starting from the S_2 system which has the lowest η . In this system $\eta = 0.2$ and silicon atoms are in average four-fold coordinated: two-fold to silicon, one- to two-fold to carbon, and one- to zero-fold to nitrogen. In this system

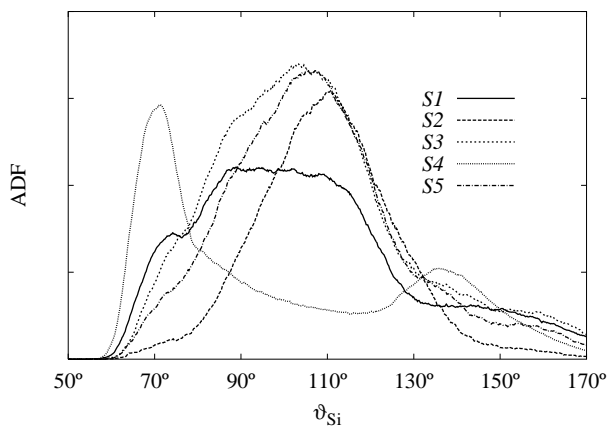


Figure 4.4: Normalized angle distribution functions of bonds originating from silicon atoms.

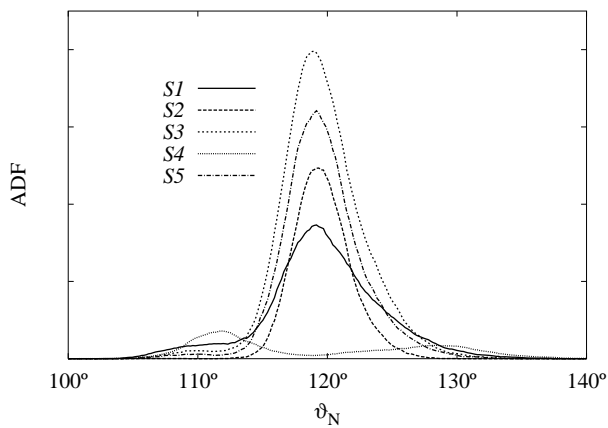


Figure 4.5: Normalized angle distribution functions of Si-N-Si bonds originating from nitrogen atoms.

Table 4.2: Percentages of Si tetrahedra in the different systems, with respect to the total number of silicon atoms.

Si(Si,C,N) ₄ structure (%)	<i>S2</i>	<i>S5</i>	<i>S3</i>	<i>S1</i>	<i>S4</i>
SiN ₄	—	12	28	21	—
SiC ₁ N ₃	1	18	13	12	—
SiC ₂ N ₂	2	9	2	6	—
SiC ₃ N ₁	3	3	—	2	—
SiC ₄	2	1	—	1	—
SiSi ₄	3	—	—	—	—
SiSi ₃ C ₁	11	—	—	—	—
SiSi ₂ C ₂	12	1	—	—	—
SiSi ₁ C ₃	6	1	—	—	—
SiSi ₃ N ₁	7	1	—	—	—
SiSi ₂ N ₂	3	4	3	—	—
SiSi ₁ N ₃	1	7	10	1	—
SiSi ₁ C ₁ N ₂	5	10	4	1	—
SiSi ₁ C ₂ N ₁	9	5	—	—	—
SiSi ₂ C ₁ N ₁	13	4	1	—	—
η	0.20	0.46	0.52	0.58	0.80

there are mainly three types of tetrahedra as reported in Table 4.2¹: SiSi₂C₂ (12%), SiSi₃C₁ (11%), and SiSi₂C₁N₁ (13%), followed by all other possible Si(Si,C,N)₄ structures. It is worth noting that this system lies on the SiC–Si₃N₄ tie-line of the ternary composition diagram in Fig. 4.1. However, nitrogen has a very low concentration and Si-Si and Si-C bonds are thus predominant.

¹in our notation the first Si atom is in the center of the tetrahedra and the following are the atoms surrounding it.

The $S5$ system has $\eta \simeq 0.46$ and corresponds to the *NCP200* material investigated in Ref. [20]. According to our calculations (Table 4.2), it consists mainly of SiC_1N_3 (18%), followed by SiN_4 (12%), $\text{SiSi}_1\text{C}_1\text{N}_2$ (10%), SiC_2N_2 (9%), and SiSi_1N_3 (7%) mixed tetrahedra. This is in agreement with Ref. [20] and with the results of J. Bill and coworkers [65], according to which silicon atoms in the *NCP200* material exist as $\text{Si}(\text{C},\text{N})_4$ mixed tetrahedra. However, in our simulations we find also $\text{Si}(\text{Si},\text{C},\text{N})_4$ as well as $\text{Si}(\text{Si},\text{N})_4$ mixed tetrahedra. Si-N bonds are preferred, followed by Si-Si and Si-C bonds in equal amount.

The $S3$ system has $\eta \simeq 0.52$ and lies on the tie-line $\text{SiC}-\text{Si}_3\text{N}_4$ of the ternary composition diagram of Fig. 4.1. In this system Si has an average total coordination number of $\simeq 4.7$. Si atoms four-fold coordinated are mainly SiN_4 (28%) and $\text{Si}(\text{C},\text{Si})_1\text{N}_3$ (13% and 10% respectively) mixed tetrahedra. The large majority of SiN_4 , the $Z(\text{Si})_{\text{N}} \simeq 3.5$, $Z(\text{N})_{\text{Si}} \simeq 3.0$, and $Z(\text{Si})_{\text{Si}} \simeq 1.0$ suggests the existence of amorphous silicon/nitrogen-rich domains made of $\text{SiSi}_x\text{N}_{4-x}$ tetrahedra, where $x=1$ on the 25% of the cases and 75% elsewhere in the domain. However this is not clear from the observation of the microstructure obtained from the simulations.

The $S1$ system has an $\eta \simeq 0.58$ and corresponds to the *VT50* material, investigated in Ref. [21]. According to our calculations, this system consists mainly of SiN_4 tetrahedra (21%), in agreement with the experimental results of Ref. [21], and partly of SiC_1N_3 (12%) mixed tetrahedra in agreement with Ref. [65] and very recent results of Ref. [16]. The large number of SiN_4 structures, together with calculated $Z(\text{Si})_{\text{N}} \simeq 4$ and $Z(\text{N})_{\text{Si}} \simeq 3$, suggest the existence of amorphous Si_3N_4 domains. This is also supported by the observation of the microstructure obtained by simulations.

The $S4$ system has an $\eta = 0.8$ and lies in the three-phase field $\text{C}-\text{Si}_3\text{N}_4-\text{N}$ (see Fig. 4.1). This system contains a large amount of seven- to eight-fold coordinated silicon atoms. The silicon atoms are exclusively coordinated to the nitrogen ones (see Fig. 4.3). The high coordination is the reason for the narrow peak in Fig. 4.4 corresponding to an average N-Si-N bond angle $\vartheta_{\text{Si}} \simeq 70^\circ$. This system contains a large quantity of “free” monoatomic nitrogen. This is a simulation artifact, due the zero

N-N attractive part of the potential. Without this initial assumption a large number of N_2 molecules would evaporate to the surface or, at very high external nitrogen pressure, would remain in the system. On the same basis, the non zero N-N interactions would compete with the N-Si ones, thus the average total silicon coordination number would be slightly lower than in this study. In the microstructure obtained by the simulations, we observe the existence of silicon/nitrogen-rich amorphous domains.

4.3.2.2 Carbon environment: local order and microstructure

The relevant partial coordination numbers of carbon, $Z(C)_{Si}$ and $Z(C)_C$, have been plotted in Fig. 4.6 as a function of the quantity $\gamma = N_C / (N_{Si}^{available} + N_C)$. This quantity is the ratio between the total number of carbon atoms and the number of available silicon atoms, and it is related to the nitrogen/silicon concentration ratio in the system. In fact, as shown in the previous section, the nitrogen atoms screen the silicon ones by surrounding them (see Fig. 4.3). The number of available silicon atoms ($N_{Si}^{available}$) is defined here as the average fraction of non-nitrogen nearest neighbors to silicon, multiplied by the total number of silicon atoms. It was calculated as follows:

$$N_{Si}^{available} = N_{Si} \cdot \left[\frac{Z(Si) - Z(Si)_N}{Z(Si)} \right] \quad (4.1)$$

where N_{Si} is the total number of silicon atoms, $Z(Si)$ is the total silicon coordination number, and $Z(Si)_N$ is the partial coordination number of nitrogen around silicon. From the plot in Fig. 4.6 we observe that $Z(C)_C$ increases and $Z(C)_{Si}$ decreases, each linearly with γ . The partial $Z(C)_N$ has not been plotted because the C-N interactions were previously set to zero. The total coordination of carbon is $Z(C)_C + Z(C)_{Si} \simeq 3$. Fig. 4.6 shows that when the concentration of carbon exceeds that of available silicon, i.e. when $\gamma \simeq 0.5$, the C-C bonds are preferred over the Si-C ones.

The calculated partial ADFs for carbon are plotted in Fig. 4.7. A narrow peak at $\vartheta_C = 120^\circ$ shows that carbon atoms are mainly sp^2 hybridized, meaning that they have trigonal planar geometries. However,

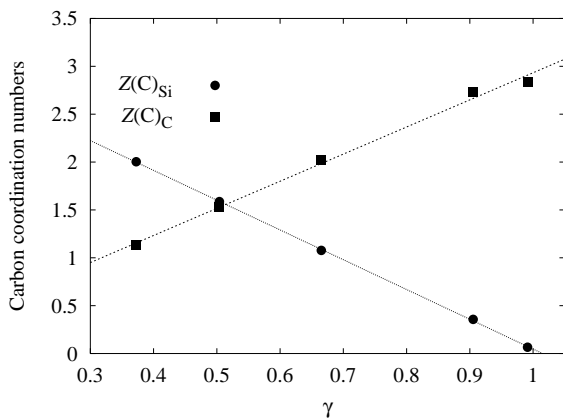


Figure 4.6: Carbon coordination as a function of $\gamma = N_C / (N_{Si}^{available} + N_C)$.

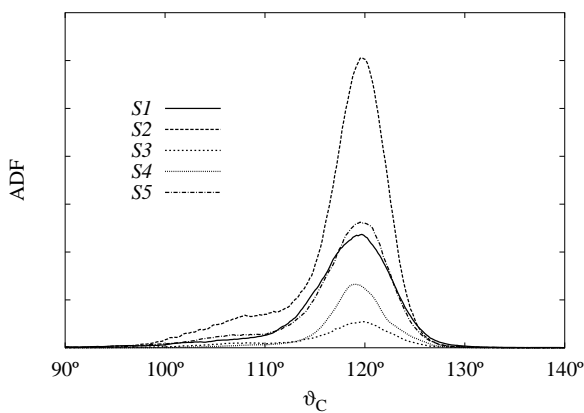


Figure 4.7: Normalized angle distribution functions of bonds originating from carbon atoms.

Table 4.3: Percentages of C structures in the different systems, with respect to the total number of carbon atoms.

system	γ	tetrahedral CSi ₄	planar			
			CSi ₃	CSi ₂ C ₁	CSi ₁ C ₂	CC ₃
<i>S3</i>	0.38	3	17	33	20	5
<i>S2</i>	0.50	2	10	34	33	12
<i>S5</i>	0.66	–	4	18	38	27
<i>S1</i>	0.90	–	–	3	20	65
<i>S4</i>	0.99	–	–	–	2	80

a shoulder due to a weak peak around $\vartheta_C = 109^\circ$ shows the existence of sp^3 hybridized tetrahedral atoms. From the partial ADFs we know that this peak is due only to C-Si bonds.

We now analyze the carbon structures starting from the system with the lowest γ . The results are summarized in Table 4.3² together with the values of γ .

In the *S3* system $\gamma \simeq 0.38$ and the carbon atoms exist mainly as planar CSi₂C₁ structures. Nevertheless, a significant percentage of carbon atoms exist as CSi₁C₂, and CSi₃ structures. Looking at the microstructure, the carbon atoms, which have a very low concentration, are homogeneously and randomly distributed in the amorphous Si-C-N network.

In the *S2* system, where $\gamma \simeq 0.5$, the carbon atoms are bonded in average to 1.5 silicon and to 1.5 carbon atoms (see Fig. 4.6). The $\simeq 34\%$ of carbon atoms exist as CSi₂C₁, $\simeq 33\%$ as CSi₁C₂, 12% as CC₃, and 10% as CSi₃ planar structures. Amorphous micro domains are not detected and carbon atoms are very homogeneously distributed.

The *S5* system, where $\gamma \simeq 0.66$, corresponds to the *NCP200* material investigated in Ref. [20]. According to our calculations $\simeq 38\%$ of the carbon atoms exist as CSi₁C₂ structures, $\simeq 27\%$ as CC₃, and $\simeq 18\%$

²in our notation the first C atom is in the center of the planar or tetrahedral structure and the following are the atoms surrounding it.

as CSi_2C_1 planar structures. Looking at the microstructure, the carbon atoms are still quite homogeneously distributed but less than in the other two previous systems.

The $S1$ system, where $\gamma \simeq 0.90$, corresponds to the $VT50$ material, investigated in Ref. [21]. According to our calculations as far as $\simeq 65\%$ of the carbon atoms exist as CC_3 planar structures. This indicates a phase separation of amorphous C-rich domains, in agreement with Ref. [10, 21] and very recent results [16]. In a very recent work [63] the energies calculated by *ab initio* calculation support a non-solubility of carbon in amorphous- Si_3N_4 , which agree with our results. The separation of the C-rich domains is evident in the microstructure displayed in Fig. 4.8.

In the $S4$ system, where $\gamma \simeq 0.99$, $\simeq 80\%$ of the carbon atoms exist as CC_3 planar structures. In this system the phase separation of a C-rich domain is almost complete. Looking at the microstructure in Fig. 4.9, we observe that the carbon atoms have crystallized into graphitic monoatomic layers forming complex bent surfaces surrounding the Si-N domains. The morphology of the structure can be described by a characteristic length l given by the ratio of the system volume to the total area of the graphite layers (computed from the number of 5-, 6-, and 7-rings). This length can be considered as the mean distance between the surfaces. For the $S4$ system we obtain $l \simeq 30 \text{ \AA}$. In order to determine the dependence of l on the system size, we have performed a large simulation with 108000 atoms using a simulation box with initial side lengths of 117 \AA . In this case we obtain $l \simeq 27 \text{ \AA}$ showing that the morphology of the layers is nearly independent of the system size. Furthermore, the separation of graphite carbon is due solely to the lack of silicon atoms, as these are completely screened by nitrogen ones. When the screening is present, graphitic monoatomic carbon layers are formed, independently of the detailed screening process of silicon atoms. This was verified performing a simulation on a monoatomic system of carbon atoms in the same thermodynamic conditions. In this way we verified that, although the $S4$ system contains some computational artifacts concerning the Si-N domains, these do not affect the results concerning the C-rich phase.

4.3.3 Summary

We have used the Tersoff potential to simulate the atomic structure of Si-C-N homogeneous materials as they are rapidly cooled from high temperatures. We have investigated the dependence of the local order on the materials composition.

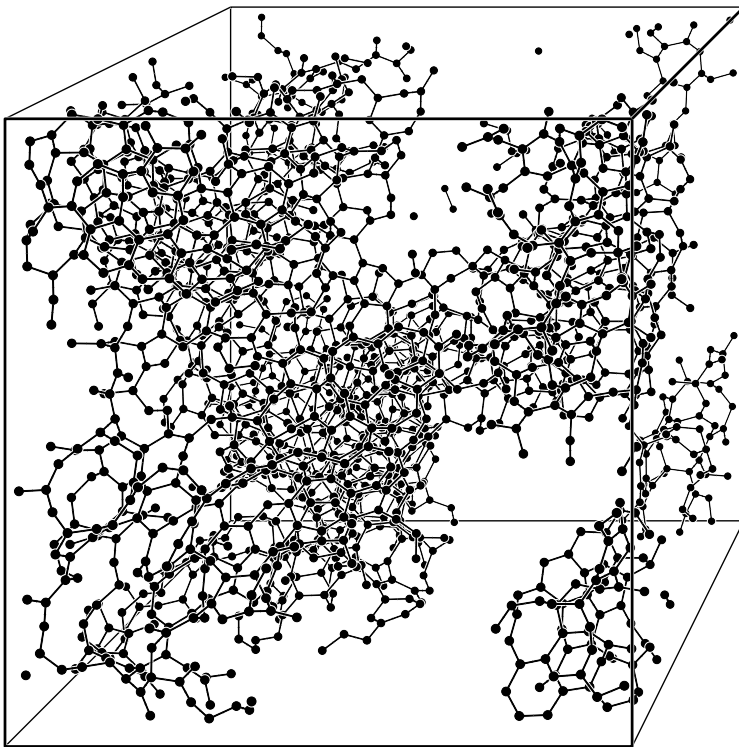


Figure 4.8: Separation into amorphous C-rich domains in the *S1* system. Only the carbon atoms are displayed. The cubic simulation box at the end of the simulated annealing has side lengths of 33 Å.

Our results predict that both the local order and the microstructure of the Si-C-N systems are determined by the stoichiometry of the material. We observe a phase separation into sp^2 hybridized C-rich and Si/N-rich domains to appear within certain composition ranges, dictated only by the nitrogen/silicon ratio.

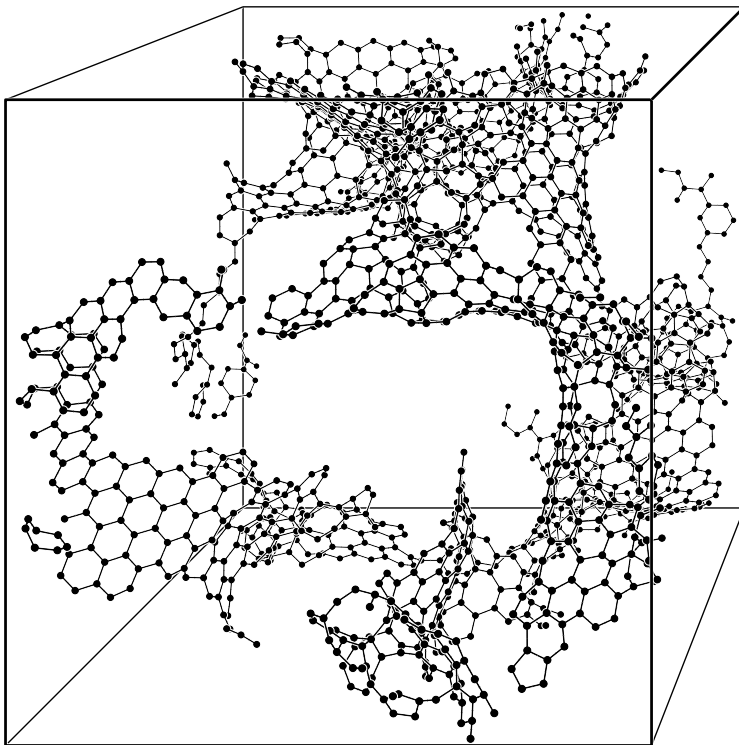


Figure 4.9: Monoatomic graphitic layers in the S_4 system. Only the carbon atoms are displayed. The cubic simulation box at the end of the simulated annealing has side lengths of 43 Å.

(1) The local structure around silicon atoms depends on the nitrogen/silicon ratio, regardless of the carbon amount. Silicon atoms are always four-fold or higher coordinated, depending on the nitrogen/silicon ratio. In agreement with Ref. [16, 20] and with results of J. Bill [65], $\text{Si}(\text{C},\text{N})_4$ mixed tetrahedra exist in a wide composition range.

In particular, a nitrogen/silicon ratio $\simeq 4/3$ leads to the predominant formation of SiN_4 tetrahedra, and thus, towards a separation of an amorphous Si_3N_4 rich phase, in agreement with Refs. [10] and [21]. However, for this ratio, mixed $\text{Si}(\text{C},\text{N})_4$ tetrahedra are also present. Below the $4/3$ ratio, silicon atoms form mainly $\text{Si}(\text{C},\text{N})_4$ and partially $\text{Si}(\text{Si},\text{C},\text{N})_4$ mixed tetrahedra. Far above the $4/3$ ratio, we find Si/N-rich domains, where Si atoms are higher than four-fold coordinated.

According to a very recent thermodynamic modeling of amorphous Si-C-N ceramics [17], the presence of these mixed tetrahedra could explain the characteristic resistance of these amorphous materials to crystallize.

(2) The local structure around carbon atoms depends on the ratio of carbon to available silicon. The availability of silicon depends on the nitrogen/silicon ratio. Carbon is always in average three-fold coordinated and is involved in mixed $\text{C}(\text{Si},\text{C})_3$ structures. Only for a sufficient high ratio of carbon to available silicon, i.e. for a sufficient high nitrogen/silicon ratio ($>4/3$), a separation of C-rich domains can be observed. If no silicon atoms are available because they are totally screened by nitrogen atoms, crystalline graphitic monoatomic layers are formed within the material. It is the first time that the formation of graphite surfaces and of C-rich domains has been simulated within a classical molecular dynamics modeling of Si-C-N amorphous systems.

4.4 Thermal Evolution

Heating and annealing amorphous Si-C-N ceramics at temperatures above ≥ 1800 K leads to phase separation, crystallization [21, 20, 11, 13, 9, 12, 16], and finally to thermal decomposition of these materials (see also Section 2.2). The process is accompanied by volume shrinkage and is most likely due to structural modifications, the atomic details of which are not completely known. It could be that the heating process causes the rearrangement of the existing bonds and leads to an increasing of the most stable ones. These are the more resistant to further diffusion. The enlargement of the amorphous domains leading to crystallization would therefore be slowed down. These suggestions are mere hypotheses at this point and much work is needed to sort out the molecular mechanisms of flow in these materials.

In this section we study the thermal evolution of one particular system, corresponding to the experimental *VT50* sample. We follow the energy, the density, the atomic mobility, and the atomic structure.

4.4.1 Method

The starting computational sample, named hereafter *RMC*, was obtained in a previous study by J. Dürr [66, 21] by means of Reverse Monte Carlo calculations. In his work, J. Dürr started from cubic clusters (box-length=40.65 Å) containing 4500 ($\text{Si}_{24}\text{C}_{43}\text{N}_{33}$) randomly distributed atoms. The stoichiometry of *RMC* system is $\text{Si}_{24}\text{C}_{43}\text{N}_{33}$, corresponding to the *S1* system of Fig. 4.1. For the Reverse Monte Carlo simulation, weighting factors were taken from X-ray and neutrons scattering data of a sample pyrolyzed at $T=1400$ K. Furthermore, additional informations about the existence of two different phases, amorphous C and amorphous Si_3N_4 , were employed as a constraint during the simulation. As result, in the atomistic configuration obtained by J. Dürr, 71% of C atoms had three direct C neighbors, 62% of the N atoms had three Si neighbors and 62% of the Si atoms had four N neighbors.

In this work we have heated the *RMC* system at constant pressure (NPT ensemble). We have started by equilibrating the system at $T=300$ K, room temperature, for 200 ps, with $P \simeq 0$ GPa. Then the temperature

was suddenly increased of $\Delta T = 230$ K and the system equilibrated for 200 ps. This procedure was continued up to $T \simeq 5000$ K, temperature by which *RMC* system was completely liquid. At each annealing temperature the system was equilibrated for 200 ps and then for a period $t = 10$ ps (10^{-11} sec). In this last equilibration period, energy, volume and pressure data were saved every 10^{-15} sec, allowing an averaging over 10^4 data. Coordinates were saved every 100×10^{-15} sec and relevant quantities were computed for each of them, giving averaged values over $\simeq 10^5$ points ($10^4/100 \times 10^3$ atoms).

4.4.2 Energy and density during annealing at high T

Figs. 4.10 and 4.11 show the potential energy and the density of the system during heating. The system reaches a minimum in its potential energy, i.e. a maximum of stability, around $T = 1800$ K, when the density of the material is $\simeq 2.46$ gcm^{-3} . Being the density of the system at room temperature $\simeq 2.17$ gcm^{-3} , we find that for the heating process, from room temperature to 1800 K, the densification is $\simeq 12\%$. We believe that this densification is due to structural rearrangements and to the reduction of the porosity but not to the reduction of the "free volume" (see Section 2.1). We believe that the difference between the density of the system in the minimum of its potential energy ($\simeq 2.46$ gcm^{-3}) and the density of the fully crystalline material ($\simeq 2.785$ gcm^{-3} for the silicon nitride/graphite composite) reflects the molecular porosity in the amorphous material, often referred to as "free volume".

At very high temperatures, the density decreases with T because of thermal expansion of the liquid. It has to be mentioned that these materials decompose before melting, giving rise to N_2 and to the stable crystalline phases. In our simulations this is not possible because the nitrogen atoms do not interact with each other, being forced to remain into the system. Moreover the simulation timescales would be in any case too short to observe structural rearrangements leading to decomposition.

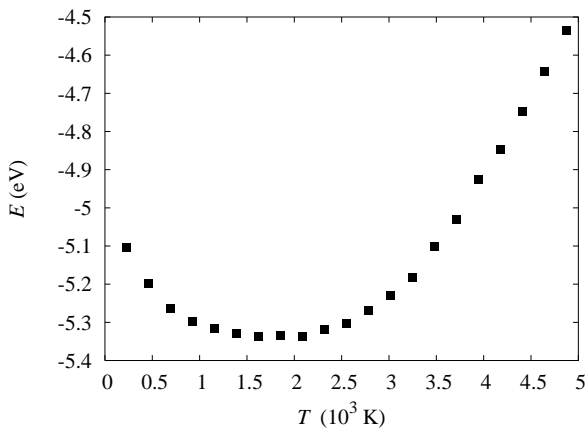


Figure 4.10: Potential energy of the system as a function of the temperature

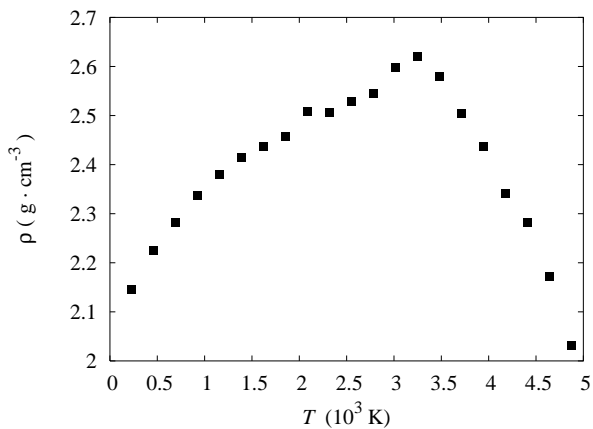


Figure 4.11: Density of the system as a function of temperature

4.4.3 Self-diffusion in amorphous Si-C-N

The enlargement of the amorphous domains and the transition to the polycrystalline material are diffusion-controlled processes. The understanding of self-diffusion, i.e. diffusion of Si, C, and N, in amorphous Si-C-N ceramics and the knowledge of the corresponding diffusion coefficients are of both scientific and technological importance. The self-diffusion mechanism and coefficients for these materials have been investigated by W. Franck [67], S. Matics [68], T. Voss [69]. The experimental diffusion coefficients range in the order of $\simeq 10^{-20} \text{m}^2 \text{s}^{-1}$ at $T \simeq 1370 \text{ K}$ (1100°C) for Si and C atoms.

By means of MD simulations, atomic diffusion can be analyzed by the calculation of the mean square displacements, defined as:

$$\langle \Delta r(t)^2 \rangle = \frac{1}{N} \sum_{i=1}^N \Delta r_i(t)^2 \quad (4.2)$$

where $\Delta \mathbf{r}_i(t)$ is the traveled distance of the particle i in time t and $\langle \Delta r(t)^2 \rangle$ is the mean square of these distances as a function of the time t . The mean square displacement is related to the diffusion coefficient D , which is a macroscopic quantity, by the Einstein relation:

$$\frac{\delta \langle \Delta r(t)^2 \rangle}{\delta t} = 6D. \quad (4.3)$$

Fig. 4.12 shows the diffusion coefficient of the Si-C-N system at different temperatures. Given a simulation period of $t \simeq 200 \text{ ps}$, a diffusion coefficient $D \simeq 10^{-10} \text{m}^2 \text{s}^{-1}$ would give rise to an atomic displacement of 2 \AA , that may already be considered as effective to modify the microstructure in the nanometer scale. According to this definition, Si, C, and N atoms start to effectively diffuse only for temperatures above $T = 2500 \text{ K}$, while below such temperature we can observe only atomic "vibrations" leading to atomic structure rearrangements but not to microstructural ones.

Nitrogen atoms are lighter than carbon and silicon and start diffusing at lower T . Although carbon atoms are not the heaviest, they are the

last to diffuse, due to the stability of the C-C bonds (see also Fig. B.2). There is a temperature range in which N atoms diffuse into the ceramic while carbon and silicon atoms are vibrating around metastable equilibrium position. In this temperature range, microstructural rearrangements occur due to the N mobility.

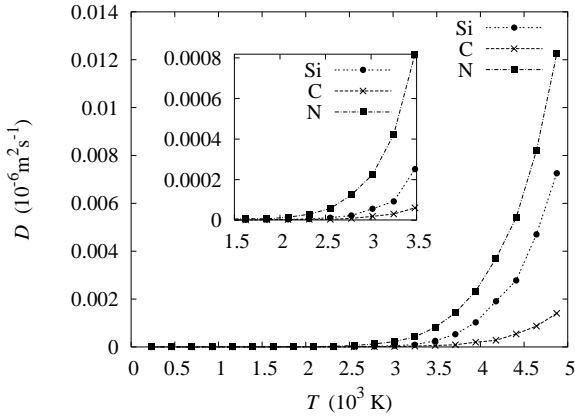


Figure 4.12: Diffusion coefficients for silicon, carbon and nitrogen atoms at different temperatures

The diffusion process follows the Arrhenius law and the diffusion coefficient can be expressed as:

$$D = D_0 e^{-\frac{H}{kT}} \quad (4.4)$$

where D_0 is a quantity related to the entropy of the process, H is the activation energy and k is the Boltzmann constant. In Fig. 4.13 the natural logarithm of the diffusion coefficient is plotted as a function of the inverse of the temperature, for high temperature, i.e. for temperature at which we can observe diffusion in our simulations. From such plot we have calculated the activation energy and the D_0 factors for the three atomic species. Results are reported in Table 4.4. These results are hardly comparable to the experimental data of Refs. [68] and [67],

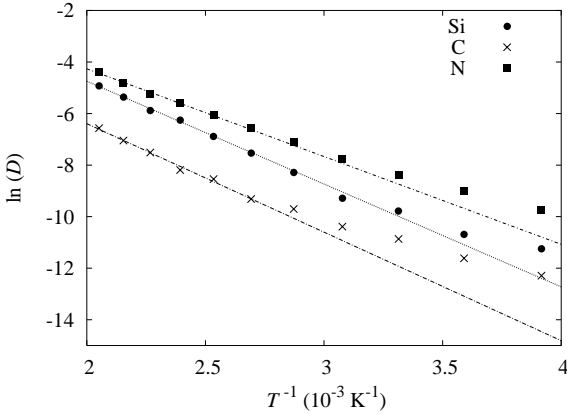


Figure 4.13: Arrhenius plot for diffusion coefficients at high temperature. The linear regression was calculated for $T \geq 3900$ K

because they refer to higher T , i.e. to the simulated "liquid". However, liquid Si-C-N cannot be obtained experimentally because it decompose previous to melting.

However, we believe that the qualitative results obtained here can hold also at lower T . In fact, the Tersoff potential does not depend on temperature and has been parameterized in order to predict the stability of structures mainly at room T . In other words we believe that in general, for every T , the C atoms are the less diffusing in the amorphous Si-C-N network. We conclude that phase separation and further crystallization is mainly to be ascribed to Si and especially to N atomic diffusion.

	D_0 [m^2s^{-1}]	H [eV]
Si	25.5×10^{-6}	3.43
C	7.6×10^{-6}	3.63
N	12.8×10^{-6}	2.94

Table 4.4: Entropy factors (D_0) and activation energies (H) for self-diffusion in amorphous Si-C-N

4.4.4 Structural evolution

Fig. 4.14 shows the partial RDF (see Section 4.2) for C-C pairs, Fig. 4.15 for Si-N pairs and Fig. 4.16 for Si-C pairs. All RDFs are plotted for six different temperatures, namely for $T=300$ K (room T), $T=1000$ K, $T=2000$ K, $T=3000$ K, $T=4000$ K, and $T=5000$ K. According to our previous calculations on the diffusion coefficient, the Si-C-N system is an amorphous ‘solid’, namely a glass, for $T \leq 3000$ K and a liquid at higher T . The RDF peak positions do not change with T and are reported in Table 4.5 together with the peaks positions in relevant crystal structures. Before calculation of the RDF, the crystal structures have been minimized by means of calculation with the Tersoff potential, with Si and C parameters from Ref. [24] and N parameters from Ref. [60] (see Appendix B).

Table 4.5: Peak positions of partial RDFs for the amorphous system and relevant crystal phases.

Material	Peak position r (Å)					
	C-C		Si-N		Si-C	
<i>RMC</i> amorphous	1.45	2.55	1.75		1.85	
beta-Si ₃ N ₄			1.70-1.76	3.1		
cubic-SiC		3.05			1.86	3.57
Graphite	1.42	2.45	2.85			
Diamond	1.55	2.51	2.95			

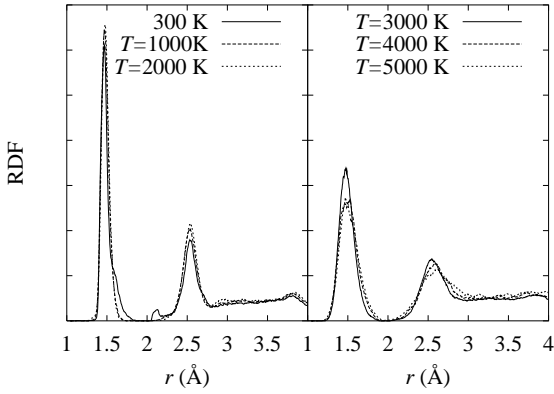


Figure 4.14: Partial C-C RDFs at different temperatures

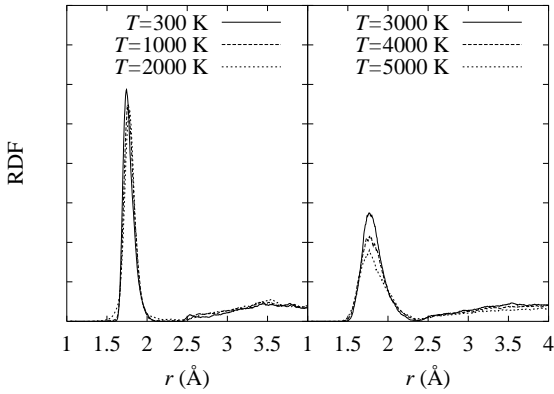


Figure 4.15: Partial Si-N RDFs at different temperatures

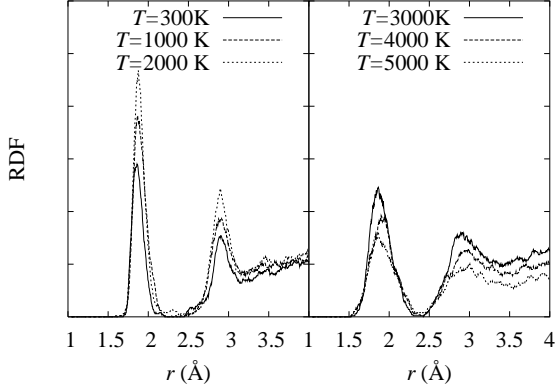


Figure 4.16: *Partial Si-C RDFs at different temperatures*

Fig. 4.17 shows the thermal evolution of the average total coordination numbers for the three atomic species. In Table 4.6 we have reported the partial coordination numbers calculated compared with experimental data [21].

Table 4.6: *Calculated partial coordination numbers*

Coordination numbers	Experimental	This work
$Z(\text{Si})_{\text{Si}}:Z(\text{Si})_{\text{C}}:Z(\text{Si})_{\text{N}}$	—:—:4.0	0.0:0.9:3.7
$Z(\text{C})_{\text{Si}}:Z(\text{C})_{\text{C}}:Z(\text{C})_{\text{N}}$	—:2.6:—	0.5:2.5:0.1
$Z(\text{N})_{\text{Si}}:Z(\text{N})_{\text{C}}:Z(\text{N})_{\text{N}}$	3.0:—:—	2.7:0.2:0.8

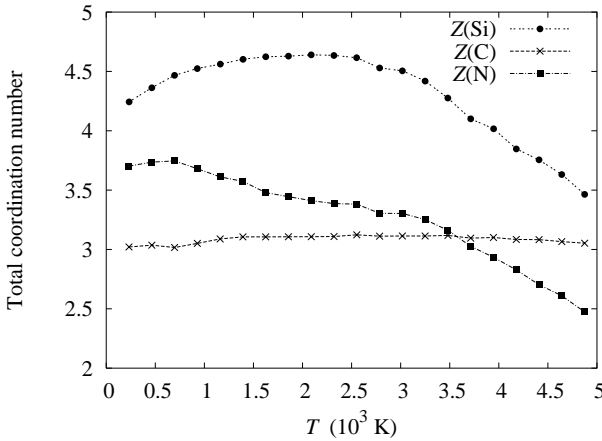


Figure 4.17: Thermal evolution of $Z(\text{Si})$, $Z(\text{C})$, and $Z(\text{N})$.

Figs. 4.18, 4.20, and 4.19 show the calculated bond angle distribution functions (ADFs) of silicon, carbon and nitrogen where a cut-off $R = 2.2 \text{ \AA}$ is used.

4.4.4.1 Silicon environment

Silicon atoms have an average total coordination number $Z(\text{Si}) \simeq 4$ that first increases with the increasing annealing temperature and then decreases for $T > 2500 \text{ K}$. Above this temperature, the Si atoms effectively diffuse. From the partial coordination numbers calculations, we know that $Z(\text{Si})_{\text{N}}$ decreases from a value of 3.7 to a value of 2.6 at higher T , while $Z(\text{Si})_{\text{C}}$ remains almost constant for all annealing temperatures. The silicon angular distribution function (ADF) is very broad, centered around a value of $\theta_{\text{Si}} = 109^\circ$, indicating that silicon atoms form tetrahedra more or less distorted, also at very high T . However, for lower T , a sharp peak around 60° is observed, due to some higher coordinated silicon structures. This is in accordance with the fact that for silicon a total coordination $Z(\text{Si}) > 4$ was found.

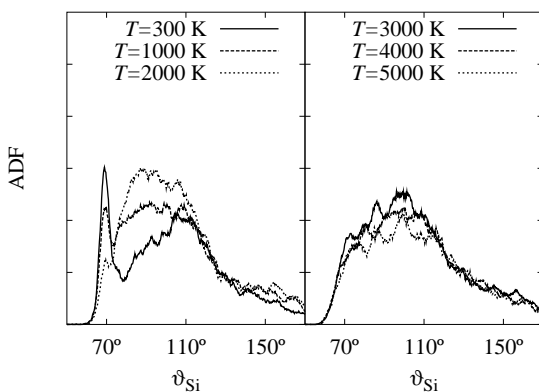


Figure 4.18: Normalized ADF of bonds originating from Si atoms

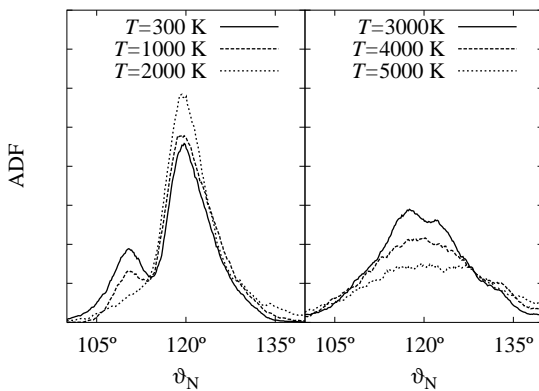


Figure 4.19: Normalized ADF of Si-N-Si bonds originating from N atoms

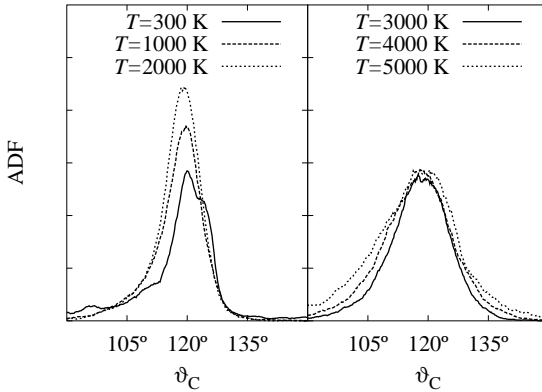


Figure 4.20: Normalized ADF of bonds originating from C atoms

Nitrogen atoms are in average more than three-fold coordinated at low temperature and less at high temperature. From partial coordination data we know that nitrogen atoms are coordinated to 2.6 silicon at low T and this coordination decreases to an average value of $Z(\text{N})_{\text{Si}} \simeq 2$ at very high temperature.

4.4.4.2 Carbon microstructure

Carbon atoms have a constant average coordination number, $Z(\text{C}) \simeq 3$ (Fig. 4.17). The carbon ADF is narrow and centered around $\theta_{\text{C}} = 120^\circ$. These two data indicate that carbon atoms form planar structures, being mainly sp^2 hybridized. Carbon atoms structures do not change during the heating at high T . This is also true for partial carbon coordination numbers.

In Fig. 4.21 percentage quantities of CC_3 , of NSi_3 and of SiN_4 structures are plotted as a function of the annealing T . From the plot and from Table 4.7 we can see that, at room temperature, only 42 % (compared to the initial 62%) of total carbon atoms form CC_3 planar structures. The number of these structures increase with increasing temperature.

Table 4.7: Percentages of Si, C, and N structures with respect to the total Si, C, and N numbers respectively.

Structures (%)	<i>RMC</i> [21]	<i>RMC</i> (this work)
SiN ₄	62	50
CC ₃	71	42
NSi ₃	62	60

The number of nitrogen atoms forming NSi₃, is similar to the one found by J.Dürr, around 60%, at room T but tend to increase up to 68% at higher T . For $T > 2500$ K this percentage abruptly decrease. The number of silicon atoms forming SiN₄ tetrahedra is around 50% and decreases with increasing temperature.

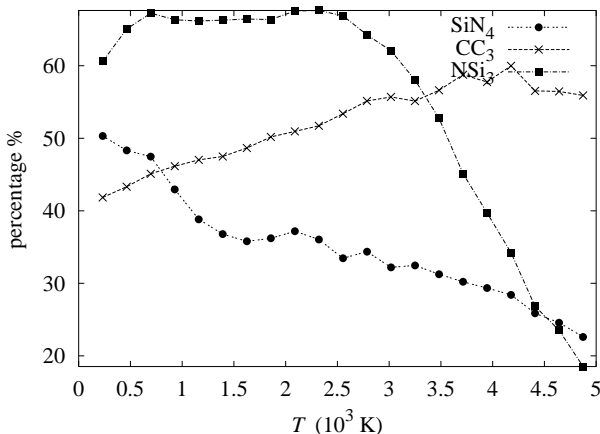


Figure 4.21: Percentage quantities of CC₃, NSi₃, and SiN₄ structures are plotted as a function of the annealing T .

4.4.5 Summary

We have used the Tersoff potential to simulate the thermal evolution of a computational sample, corresponding to the $\text{Si}_{24}\text{C}_{43}\text{N}_{33}$ ceramic, obtained by J. Dürr through a Reverse Monte Carlo simulation [66, 21]. The potential energy and density have been followed during heating. Volume shrinkage, as observed experimentally, occurs and we calculate a densification of $\simeq 12\%$ of the material heated from room T up to 1800 K. Diffusion coefficients have been calculated. We calculate the activation energies for the atomic diffusion and find that carbon is the slowest atomic specie in the amorphous network. Phase separation therefore occurs mainly because of Si and especially of N mobility.

Silicon, carbon, and nitrogen environments were investigated by calculating the radial and angular distribution functions at all temperatures, as well as the coordination numbers. According to our calculations, the configuration obtained by Reverse Monte Carlo Technique was not an equilibrium amorphous solid and we observe structural changes already by equilibrating at room T . In our simulation the phase separation is less pronounced than as predicted and assumed in Ref. [21]. It has to be mentioned, however, that the *RMC* density as obtained by J. Dürr is $\rho = 1.85 \text{ gcm}^{-3}$. After equilibrating by MD simulation at room temperature ($T = 300 \text{ K}$) and constant pressure ($P = 0 \text{ GPa}$) for $t = 200 \text{ ps}$, the density increases up to $\rho = 2.17 \text{ gcm}^{-3}$. This increase of density at room temperature changes the atomic structure of the *RMC* sample created by J. Dürr. The densification at room temperature is due to the fact that simulations have been carried at $P = 0 \text{ GPa}$, while in calculations performed by J. Dürr the density of the material was assumed to be constant and equal to the experimental one. The experimental density is a mean density of bulk dense material and pores. In fact, the Si-C-N ceramics “as pyrolyzed” are porous and the physical nature of the porosity can be classified in three ways. The first two types can be addressed to as open and close porosity, while the third type is usually referred to as “free volume”. In MD simulations at zero iso-static pressure, open pores are not stabilized, and disappear after simulated annealing, giving rise to a densification process. We believe that the close pores and the “free volume” remains after simulated equilibration at room temperature. On the other hand we believe that the densification occurring

after heat treatment is due to the elimination of the close porosity and not to the elimination of free volume. The “free volume” has here been estimated to be related to the difference between the density of the amorphous having the lowest potential energy ($\simeq 2.46 \text{ gcm}^{-3}$) and the density of the fully crystalline material ($\simeq 2.78 \text{ gcm}^{-3}$ for the silicon nitride/graphite composite). However, the exact computation of the “free volume” from the atomic structures has not been calculated and we believe that this could be an interesting outlook of this thesis.

Simulations of crystal growth

The crystallization behavior of polymer-derived Si-C-N ceramics that contain residual open porosity can be described by a stepwise change in the microstructure initiated by the rearrangement of the polymer network structure during heat treatment, which yields phase separation in the amorphous state. According to J. Kleebe [11] the formed N-rich domains tend to decompose at higher temperatures creating N-depleted, Si-C-enriched regions within the bulk. The change in local chemistry promotes crystallization of cubic (β -)SiC. The formation of vapor phases (escape of nitrogen) support outer and inner surface crystallization.

Phase transition crystallization processes can be difficult to observe in MD simulations. One of the reasons is the limitation in time and length scale available. In Si/C materials, diffusion of atomic species such as Si and C are very slow, in the order of $\simeq 10^{-20}\text{m}^2\text{s}^{-1}$ at $T \simeq 1370\text{K}$ (1100°C) [67, 68]. The structural rearrangement leading to the nucleation of critical SiC crystalline seeds to promote further growth are therefore very unlikely to be observed in a typical MD simulation. A less complex phenomena is the crystal growth once the primary seeds are formed within Si/C amorphous domains. In this work we investigate the atomic mechanisms involved in silicon carbide crystal growth. In order increase the kinetics of the process and to reduce the simulation times, we perform the simulations at high pressure.

Moreover, before attempting the SiC crystal growth simulations, it is necessary to demonstrate that empirical potentials can predict crystallization processes in complex covalent two-component compounds. For this reason, we have begun by considering a simple case: Diamond crystal growth.

5.1 Crystal growth of diamond

Synthetic diamond is formed commercially using high pressure [70] and other processes like chemical-vapor deposition and shock-wave, having serious limitations owing to low production volumes and high costs.

Here we study the crystal growth of diamond from amorphous carbon at high pressure, when a crystal seed is included into the material.

5.1.1 Method

The molecular dynamics calculations in this work are performed in the NVT (constant particle number, constant volume, and constant temperature) ensemble. The covalent atomic interactions are modeled by the Tersoff many-body classical potential [23] with carbon parameters from ref. [24] (see Appendix B). The MD simulations are performed using supercells initially consisting of a crystal diamond seed in contact with the amorphous carbon. Different diamond seeds are considered: having different shapes, dimensions and in presence of defects. All the initial supercells contain a crystalline/amorphous interface. Periodic boundary conditions are applied in all directions. The supercells consist of 1000 to 2000 atoms and have atomic density of $0.177 \text{ atoms}/\text{\AA}^3$ (3.536 g/cm^3). The initial c/a interfaces are obtained by heating diamond supercells while keeping the atoms of the desired seed artificially fixed. The resulting two-phase systems, consisting of a crystalline “cold” phase and a liquid “hot” phase, are then equilibrated for 20 ps, corresponding to 10^4 time steps, at very high temperature, $T \simeq 2 \times 10^4 \text{ K}$. The annealing simulations are then performed at temperatures ranging from $T \simeq 0.1 \times T_m$ to $T \simeq 0.7 \times T_m$, where T_m is the simulated melting temperature of diamond at constant volume.

In the following sections we describe the results for the three different simulation sets.

5.1.2 Annealing at different temperatures

We anneal a supercell containing 2000 atoms and consisting of a crystalline diamond layer of thickness $\simeq a$ ($a = 3.56 \text{ \AA}$ is the lattice constant given by the Tersoff potential) in contact with an amorphous layer of thickness $\simeq 9 \times a$. Since periodic boundary conditions are applied in all directions, two equivalent crystalline/amorphous (c/a) interfaces are included in the supercell. The crystalline interfacial plane have the orientation $\{100\}$.

Snapshots of a simulation at $T \simeq 0.45 \times T_m$ are displayed in Fig. 5.1: before the annealing, after 30 ps, and after 60 ps. The c/a interface displacement in the $\langle 100 \rangle$ direction can be observed. At the considered annealing temperature, the crystallization is completed after 120 ps.

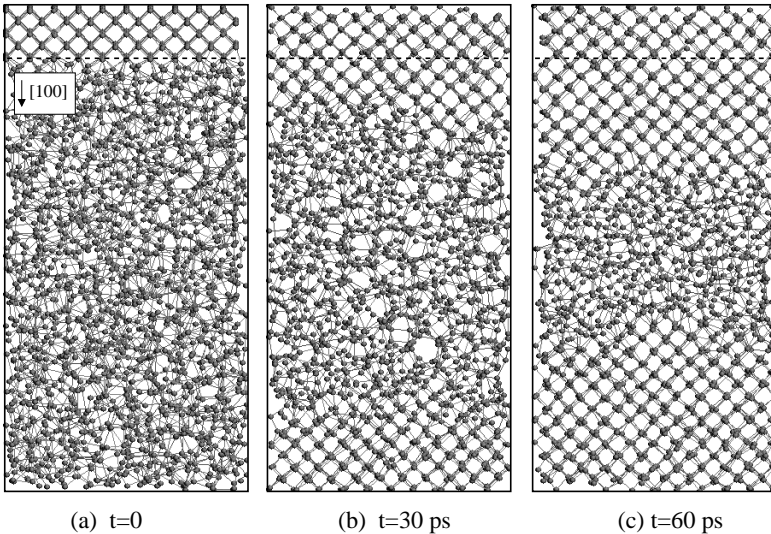


Figure 5.1: Snapshots of the MD supercell during annealing at $T \simeq 0.45 \times T_m$. The dashed line shows the initial c/a interface position.

We perform several annealing simulations of the same initial supercell at different temperatures. Annealing temperatures range from $T \simeq 0.30 \times T_m$, at which no crystallization is observed for $t < 2000$ ps, to $T \simeq 0.70 \times T_m$, leading to the complete melting of the seed. It is worth noticing that all simulations are performed at the same constant atomic density of $0.177 \text{ atoms}/\text{\AA}^3$. In this way, the isostatic pressure in the system ranges from $P \simeq 100 \text{ GPa}$ to $P \simeq 150 \text{ GPa}$ with the increasing temperature. We calculate the crystal growth rate by plotting the potential energy as a function of the annealing time. To do this, we assume that the crystallization proceeded along the $\langle 100 \rangle$ direction, perpendicular

to the $\{100\}$ crystal plane. This assumption seems to be realistic by the simple observation of the simulation snapshots. Fig. 5.2 shows the Arrhenius plot of the growth rates. By linear fitting of the simulated data we calculate an approximate activation energy, $E \simeq 2.9$ eV, for the crystal growth process. However, this is a rough estimation because we don't analyze in detail the atomistic mechanism responsible for the crystallization process. The specific mechanism could also consist of many steps with different activation energies. Furthermore it could be that at different temperature regimes, different crystallization paths are followed. However, a detailed analysis of the crystal growth of diamond from the amorphous is outside the scope of this thesis.

5.1.3 Diamond crystal seed with twin grain boundaries

As in the previous simulated annealing, the initial supercells contain $\simeq 2000$ atoms and consist of a crystal layer seed in contact with the amorphous carbon. The crystal seed in the initial supercells contains two tilt grain boundaries each, perpendicular to the c/a interface. We study three different systems which include three different types of grain boundaries: the first, named $GB111$ hereafter, includes two $\langle 111 \rangle$ tilt grain boundaries ($\Sigma = 3$, (111) , 70.53°), the second system, $GB120$, includes two $\langle 110 \rangle$ tilt grain boundaries ($\Sigma = 9$, (221) , 38.94°), and the third system, $GB221$, includes two $\langle 001 \rangle$ tilt grain boundaries ($\Sigma = 5$, (120) , 36.87°). Periodic boundary conditions are applied in all directions, in this way each initial supercell contains two c/a interfaces. The systems created in this way are annealed at $T \simeq 0.60 \times T_m$ for $t \simeq 300$ ps, after which the crystallization is complete. In Figs. 5.3, 5.4, and 5.5 the initial and the crystallized systems are displayed for the three supercells with different grain boundaries. The dashed lines correspond to the initial positions of the tilt grain boundaries. We can observe that all systems crystallize but several defects occurs into the final structure. In particular, the only crystal seed which maintains the initial tilt grain boundary is the $GB111$ system.

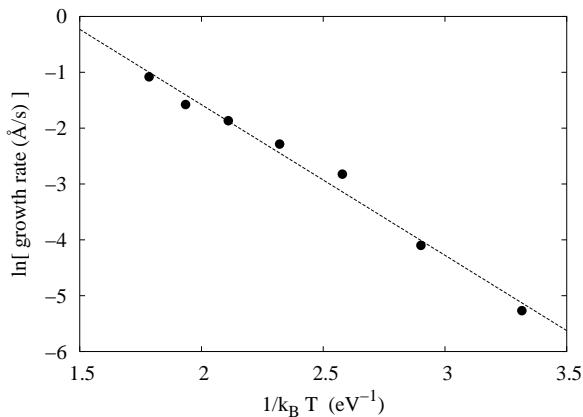


Figure 5.2: Arrhenius plot of the growth rates.

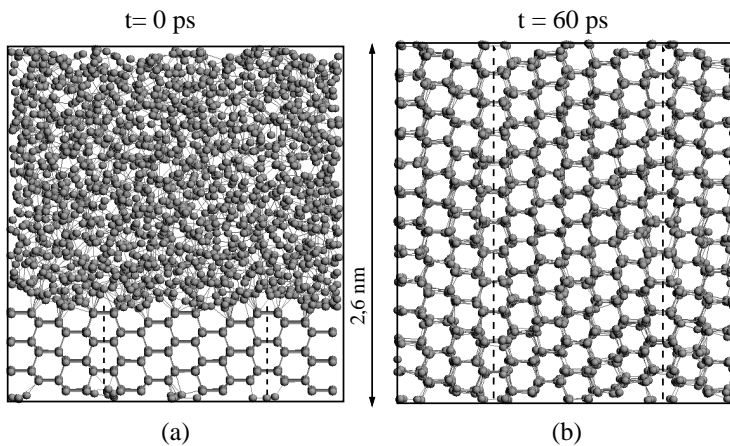


Figure 5.3: GB111 system before (a) and after (b) the simulated annealing at $T \simeq 0.60 \times T_m$. The dashed lines show the position of the two $\langle 111 \rangle$ tilt grain boundaries ($\Sigma = 3$, (111) , 70.53°) before the annealing.

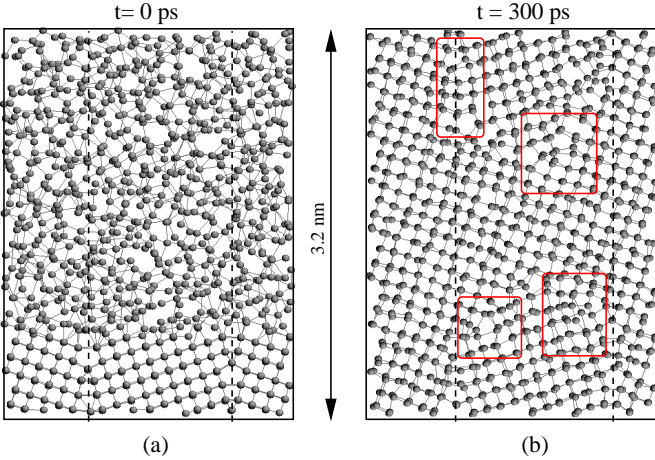


Figure 5.4: *GB120* system before (a) and after (b) the simulated annealing at $T \simeq 0.60 \times T_m$. The dashed lines show the position of the two $\langle 110 \rangle$ tilt grain boundaries ($\Sigma = 9$, (221) , 38.94°) before the annealing. Boxes in (b) surround defects after crystallization.

5.1.4 Different shapes of the diamond seed

In this section we report the results of the annealing of five different MD supercells at different temperatures. All supercells are cubic with side length $= 5 \times a$ and contained 1000 atoms. The crystal seeds in the five systems are chosen to have different dimensions: The dimensions of the crystal seeds schematically drawn in Fig. 5.6 are $5 \times 5 \times 1 \times a$ (a), $4 \times 5 \times 1 \times a$ (b), $3 \times 5 \times 1 \times a$ (c), $2 \times 5 \times 1 \times a$ (d), and $1 \times 5 \times 1 \times a$ (e). Periodic boundary conditions are applied in all directions in way that the largest crystal seed corresponds to an infinite monolayer and the smallest to a infinite “nanowire”.

After annealing the five supercells at different temperatures we find that for increasing dimensions of the seed, going from the “nanowire” to the infinite monolayer, there is a maximum temperature above which the crystal seed melts. The smallest seed (Fig. 5.6(e)) melts at all investigated temperatures. In Fig. 5.7 we plot the normalized melting temper-

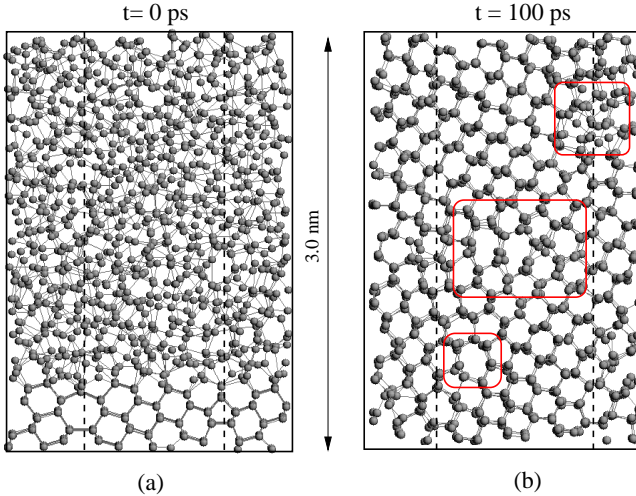


Figure 5.5: *GB221 system before (a) and after (b) the simulated annealing at $T \simeq 0.60 \times T_m$. The initial crystal seed layer contains two $\langle 001 \rangle$ tilt grain boundaries ($\Sigma = 5$ (120) 36.87°). Boxes in (b) surround defects after crystallization.*

ature of the crystal seed as a function of the surface/volume ratio of the seeds, Ω , for the four systems of Fig. 5.7 ((a), (b), (c), and (d)). Below these temperatures, all systems, except (e), crystallize after annealing for a long enough period. The melting temperature of the seed is normalized over the simulated melting temperature of diamond, obtained by slowly heating diamond at constant volume (NVT ensemble), namely at the constant atomic density of $\rho = 0.177 \text{ atoms}/\text{\AA}^3$ (3.536 g/cm^3).

5.1.5 Summary

These successful simulations on the diamond crystallization, together with results of Ref. [71] on silicon crystallization, show that the Tersoff potential is appropriate to describe the crystallization of these two mono-component (silicon and carbon) covalent systems in the cubic symmetry. These results allow us to simulate the crystallization of the two-

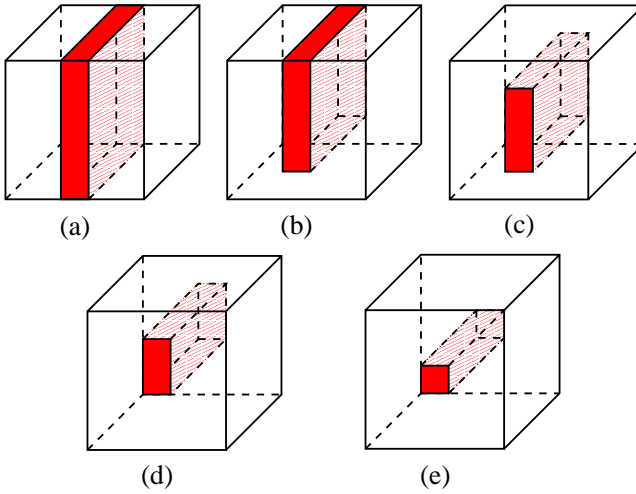


Figure 5.6: Schematic draw of the five initial MD supercells. The shadowed region corresponds to the crystalline one.

component system. In the next part we simulate the cubic SiC crystal growth process, which is involved in the crystallization of the amorphous SiCN ceramics.

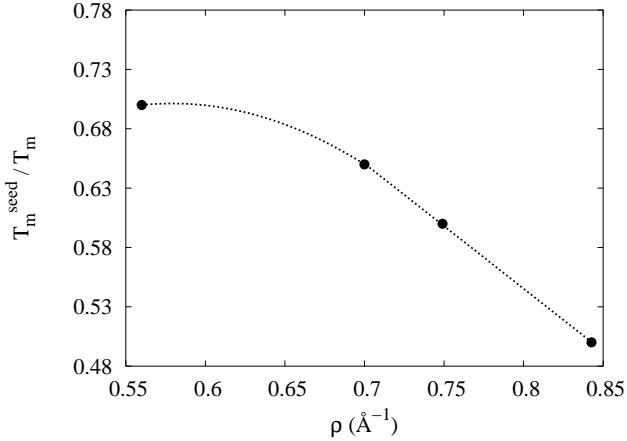


Figure 5.7: Normalized melting temperature of the crystal seed as a function of the surface/volume ratio of the seed, Ω .

5.2 Crystal growth of cubic SiC

Besides the crystallization process of the amorphous Si-C-N ceramics, the crystallization of cubic SiC from the amorphous material is a problem of general scientific interest. In fact, among the different SiC polytypes, crystalline cubic SiC is a widely applied ceramic, having high values of electron mobilities, critical electric field, and thermal conductivity. It can be grown from different phases: gas, liquid (melted silicon), and solid (amorphous). In most cases, SiC crystals are grown by a sublimation process assisted by physical vapor transport.

5.2.1 Method

The calculations in this work are performed in the NPT (constant particle number, constant pressure, and constant temperature) and in the NVT (constant volume instead of constant pressure) ensembles. The MD simulations are performed using supercells initially consisting of a crystalline SiC layer (thickness $\simeq 3 \times a$, where $a = 4.3185 \text{ \AA}$ is the lat-

tice constant given by the Tersoff potential) in contact with an amorphous SiC layer (thickness $\simeq 4.5 \times a$). Periodic boundary conditions are applied in all directions. Three crystal orientations are considered in order to obtain different crystalline/amorphous (c/a) interfaces leading to the four supercells shown in Fig. 5.8. The first supercell, shown in Fig. 5.8(a) and denoted by 100 , contains two c/a interfaces which have the same orientation of the crystalline interfacial planes, namely the $\{100\}$ planes, but differ in the composition of the terminating crystalline layers: one is carbon, the other is silicon terminated. This non-equivalence is due to the lack of a mirror symmetry operation with respect to $\{100\}$ planes in cubic SiC. The second supercell, 110 shown in Fig. 5.8(b), contains two equivalent c/a interfaces, corresponding to two equivalent crystal interfacial $\{110\}$ planes. The third supercell, $S111$ shown in Fig. 5.8(c), contains two non-equivalent c/a interfaces corresponding to the $\{111\}$ planes terminated by carbon and by silicon, both single bonded to the bulk. The cubic SiC does not possess a mirror symmetry operation with respect to the $\{111\}$ plane. Accordingly, the fourth supercell $T111$, shown in Fig. 5.8(d), contains two non-equivalent c/a interfaces corresponding to the $\{111\}$ planes terminated by carbon and by silicon atoms, both triple bonded to the bulk.

The typical initial MD supercell size is $\simeq 30 \times 30 \times 20 \text{ \AA}^3$ and contains $\simeq 2000$ atoms. The initial c/a interfaces are prepared by heating the crystalline supercells at constant volume while keeping the atoms of the crystal seed with the desired interfaces artificially fixed. The resulting two-phase systems are then equilibrated for 20 ps, corresponding to 10^4 time steps, at very high temperature, $T \simeq 10^4$ K, and pressure, $P \simeq 100$ GPa. This prevents the decomposition of SiC at high T into liquid Si and graphite, and promotes the crystallization kinetic therefore reducing the simulation time. The annealing simulations are performed in the NPT ensemble with $T \simeq 0.6 \times T_m$, where T_m is the simulated melting temperature at the given pressure, for 20-80 ns corresponding to $1-4 \times 10^8$ time-steps. During the annealing simulations, all atoms — including the ones belonging to the crystal seed — are relaxed. The atomic positions are averaged every 5×10^4 time-steps over 10^3 configurations.

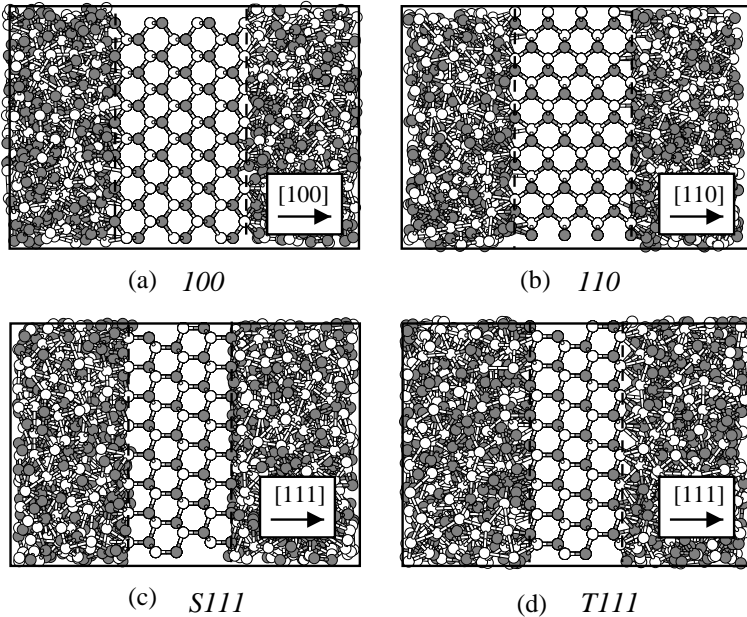


Figure 5.8: Four MD supercells containing a crystal seed layer in contact with the amorphous layer. Three different crystal orientations leading to seven different c/a interfaces are displayed, (a) $\{100\}$ -Si and -C, (b) $\{110\}$, (c) single-bond $\{111\}$ -Si and -C, and (d) triple-bond $\{111\}$ -Si and -C. In this picture, C atoms are dark while Si atoms are light.

5.2.2 Results

Crystallization is observed in the 110 , $S111$, and $T111$ supercells but not in the 100 . In order to analyze the crystallization process, we need to identify the ‘crystalline’ atoms and the ‘amorphous’ ones. For this purpose we apply a geometric criterion. Apart from few exceptions, this criterion allow us to identify the crystalline atoms for every configuration during the annealing. A ‘crystalline’ atom is defined here by the following two conditions:

- 1) The atom has four nearest neighbors within a radial cut-off of 2.2 Å.

2) The scalar products of any two bond vectors have a value between $min = (1.5\text{\AA})^2 \cos(109^\circ)$ and $max = (2.2\text{\AA})^2 \cos(109^\circ)$.

Fig. 5.9 shows a snapshot of the crystalline atoms in the different super-cells after averaging over 5×10^4 time steps. From Fig. 5.9(a), it can be seen that the 100 supercell does not crystallize because no crystal layers are formed on the initial c/a interfaces.

Crystallization is observed in the 110 supercell as shown in Fig. 5.9(b). The displayed atomic configuration corresponds to the 110 supercell after $\simeq 80$ ns of annealing. We observe that c/a interfaces, which are

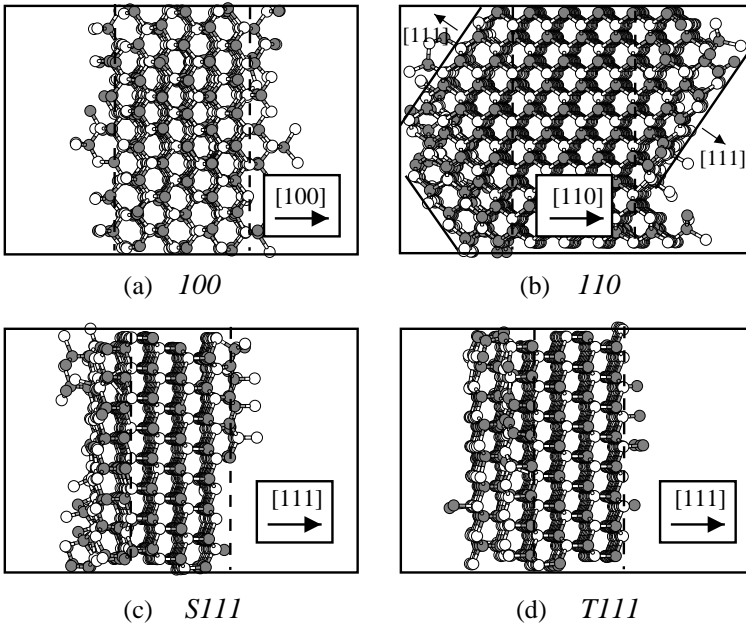


Figure 5.9: The four MD cells of figure 5.8 after annealing. Only the crystalline atoms and first neighbors are displayed. The position of the c/a interfaces before the annealing are shown as dashed lines: a) $\{100\}$ -Si and -C, b) $\{110\}$, c) single-bond $\{111\}$ -Si and -C, and d) triple-bond $\{111\}$ -Si and -C.

formed after the annealing, show a common atomic structure, that is, the new interfacial crystal atoms lay in the $\{111\}$ planes and are silicon atoms triple-bonded to the bulk. The thickness of the crystallized part in this supercell is the largest, when compared with the other three systems. We conclude that the preferred growth direction is along $\langle 110 \rangle$, perpendicular to the $\{110\}$ planes, but the growth proceeds by faceting parallel to the $\{111\}$ crystal planes. This is in agreement with the experimental results of Ref. [72]. Furthermore, according to Ref. [73], in the final CVD growth forms of cubic SiC, the silicon terminated interfaces should dominate and should have a better crystalline character, in agreement with our results.

Crystal growth is observed only for one of the two non-equivalent c/a interfaces of the $S111$ supercell as shown in Fig. 5.9(c), namely for the silicon-terminated one. The first layer that crystallizes is the triple-bonded carbon layer, followed by the single bonded carbon layer, instead of the silicon one. This produces the formation of a twin grain boundary and leads to the crystallization of a triple-bonded silicon layer which interrupts the crystallization process. The same is observed for the $T111$ supercell as shown in Fig. 5.9(d). Crystal growth is observed only for one of the two non-equivalent c/a interfaces, namely for the carbon terminated one. After the growth of four crystalline atomic layers the growth is interrupted by the formation of twin grain boundaries which produced the final c/a interface including the $\{111\}$ triple-bond silicon atoms.

5.2.3 Summary

In this part we have simulated the crystal growth of cubic SiC from the amorphous state. We have observed crystallization for the crystalline/amorphous interfaces for the interfacial crystal $\{110\}$, single-bond $\{111\}$, and triple-bond $\{111\}$ orientations. We have found that all interfaces after the annealing have a common atomic structure: Silicon $\{111\}$ layers, triple bonded to the bulk, are observed for all the interfacial crystalline atoms. We have concluded that this interface does not crystallize and its formation is responsible for the interruption, or, more probably, for a strong slowing down, of the crystal growth process. Among the three supercells which crystallized, we have observed that

the supercell containing the $\{110\}$ interfacial plane is the one that shows the largest number of crystallized atoms after the annealing. We conclude that the preferential growth directions are $\langle 110 \rangle$ but the crystal growth proceeds by faceting on the $\{111\}$ planes.

Our results are in good agreement with the experimental results of Refs. [72] and [73], both obtained with the chemical vapor deposition technique (CVD).

This work could be extended in several ways, in particular it would be of interest to calculate the crystalline/amorphous interfacial energies. It would also be of interest to calculate the growth rate of silicon and carbon in order to determine the rate limiting step.

Conclusions and Outlook

In this thesis the transformation from the amorphous Si-C-N ceramic to the polycrystalline material have been studied by isolating its fundamental steps. We have investigated the atomic structures of homogeneous amorphous Si-C-N ceramics, their thermal evolution, and we have studied the atomic mechanisms leading to the crystal growth of one of its crystalline phases, cubic SiC.

In the first part we have studied the dependence of the atomic structure on the chemical composition of Si-C-N and we have observed a separation into sp^2 hybridized C-rich and Si/N-rich amorphous domains. This separation depends only on the nitrogen/silicon ratio, regardless of the carbon amount. The Si/N-rich phase is generally made of mixed tetrahedra. In particular, for a stoichiometric nitrogen/silicon ratio of $\simeq 4/3$, silicon atoms form mainly SiN_4 and mixed $Si(C,N)_4$ tetrahedra. Below this ratio, the material is composed mainly of $Si(C,N)_4$ and partially of $Si(Si,C,N)_4$ mixed tetrahedra as well as planar $C(C,Si)_3$ mixed structures, homogeneously spread within the material. Far above the $4/3$ ratio, we find Si/N-rich domains, where Si atoms are higher than four-fold coordinated. Very interesting is the formation, in this composition range, of C monoatomic graphitic layers within the C-rich phase of the material.

The persistency, in a large Si-C-N ceramic composition range, of the mixed $Si(C,N)_4$ tetrahedra could explain why these materials are resistant to crystallization up to rather high temperatures. Furthermore, the formation of graphitic monoatomic layer observed in our simulations, could account for a further decrease of the atomic mobility and therefore for a retardation of the crystallization process at high temperatures. In another set of simulations we have followed the thermal evolution of a particular Si-C-N system, corresponding to the experimental VT50 sample. When the system is heated from room temperature up to 1800 K the volume shrinks by $\simeq 12\%$ leading to a dense amorphous material in a potential energy minimum. We estimate that the difference between this density ($\simeq 2.46 \text{ gcm}^{-3}$) and the density of the fully crystalline material ($\simeq 3.2 \text{ gcm}^{-3}$ for the silicon nitride/silicon carbide composite) is

related to the molecular porosity, i.e. to the "free volume" of the ceramic. The atomic diffusion coefficients during the heating have been calculated. Carbon atoms have the highest activation energy for the diffusive process. Phase separation therefore occurs mainly because of Si and especially of N mobility.

In the second part we have studied the crystal growth of cubic SiC from the amorphous. Before attempting the crystal growth simulations, it was necessary to demonstrate that empirical potentials could predict crystallization processes in complex covalent compounds. A preliminary analysis of the crystallization process in carbon systems yielded already unexpected results. These results together with literature data on silicon crystallization [71] have shown that this method is able to describe the crystallization of these two mono-component (silicon and carbon) covalent systems in the cubic symmetry. We have therefore investigated the microscopic mechanisms involved in the crystal growth of β -SiC from the amorphous. We have found that crystal growth proceeds by preferential crystal planes orientation and that silicon terminated surfaces are formed.

The results obtained are in good agreement with the experimental data. Moreover, they predict the behavior of these materials also in conditions far from the experimental ones. This work opens therefore new perspectives for the study of covalent ceramics by classical MD simulations. For example, the effect of mechanical stress on the microstructure of amorphous and polycrystalline Si-C-N [27, 32, 34, 35, 36, 44, 45], as well as the atomic processes involved in oxidation processes [29, 31] are open relevant questions.

Moreover, it has recently been discovered that Si-C-N ceramics containing boron synthesized by precursor polymers, show an increased thermal stability compared to the ternary Si-C-N ceramics [38, 39]. However, the microstructure of the amorphous Si-B-C-N materials, as well as the atomic mechanisms involved in their crystallization and under mechanical stress are not completely known although extensive experimental studies [40, 41, 74, 75, 76, 77, 78, 79, 80, 81, 82, 83]. Very preliminary simulations of Si-B-C-N systems have been carried out, with the aim of studying the reliability of the modeling potential when

boron atoms are included in the Si-C-N system.

Appendix

A Verlet algorithm

The numerical integration of the equations of motion is done by a time integration algorithm. This is based on a finite difference method, where time is discretized on a finite grid, the time step Δt being the distance between consecutive points on the grid. Knowing the positions and some of their time derivatives at time t , the integration scheme gives the same quantities at a time $t + \Delta t$. By iterating the procedure, the time evolution of the system, namely the trajectory of all atoms, is followed. All integration algorithms are approximate and two major problems arise:

- *Truncation errors*, related to the accuracy of the finite difference method with respect to the true solution. Finite difference methods are usually based on a Taylor expansion truncated at some term. These errors do not depend on the implementation: they are intrinsic to the algorithm.
- *Round-off errors*, related to errors associated to a particular implementation of the algorithm. for instance, to the finite number of digits used in computer arithmetics.

Both errors can be reduced by decreasing Δt .

in this work the equations of motion are solved using the Verlet algorithm, probably the most commonly used time integration algorithm for MD simulations. The basic idea is to write two third-order Taylor expansions for the positions $\mathbf{R}(t)$, one forward and one backward in time. Calling \mathbf{v} the velocities, \mathbf{a} the accelerations, and \mathbf{b} the third derivatives of \mathbf{R} with respect to t , one has:

$$\mathbf{R}(t + \Delta t) = \mathbf{R}(t) + \mathbf{v}(t)\Delta t + (1/2)\mathbf{a}(t)\Delta t^2 + (1/6)\mathbf{b}(t)\Delta t^3 + O(\Delta t^4) \quad (\text{A.1})$$

$$\mathbf{R}(t - \Delta t) = \mathbf{R}(t) - \mathbf{v}(t)\Delta t + (1/2)\mathbf{a}(t)\Delta t^2 - (1/6)\mathbf{b}(t)\Delta t^3 + O(\Delta t^4) \quad (\text{A.2})$$

Adding the two expressions gives

$$\mathbf{R}(t + \Delta t) = 2\mathbf{R}(t) - \mathbf{R}(t - \Delta t) + \mathbf{a}(t)\Delta t^2 + O(\Delta t^4) \quad (\text{A.3})$$

This is the basic form of the Verlet algorithm. since we are integrating Newton's equations, $\mathbf{a}(t)$ is just the force divided by the mass, and the force is in turn a function of the position $\mathbf{R}(t)$:

$$\mathbf{a}(t) = -(1/m)\nabla V(\mathbf{R}(t)) \quad (\text{A.4})$$

The truncation error of the algorithm is of the order of Δt^4 . This algorithm is at same time simple to implement, accurate and stable.

A problem with this algorithm is that velocities are not directly generated. While they are not needed for the time evolution, their knowledge is sometimes necessary. Moreover, they are required to compute the kinetic energy K , whose evaluation is necessary to test the conservation of the energy $E = K + V$, one of the most important tests to verify that a MD simulation is proceeding correctly. The velocities are calculated as follows:

$$\mathbf{v}(t) = \frac{\mathbf{R}(t + \Delta t) - \mathbf{R}(t - \Delta t)}{2\Delta t} \quad (\text{A.5})$$

The equations of motion in this work were integrated using the velocity-Verlet algorithm with a time step $\Delta t = 0.2$ fs.

B Tersoff Potential

For a multicomponent system, the Tersoff potential energy E , as a function of the atomic coordinates, is taken to be [24]:

$$E = \sum_i E_i = \frac{1}{2} \sum_{i \neq j} V_{ij} \quad (\text{B.6})$$

where V_{ij} is the interaction energy between atoms i and j and is a combination of repulsive and attractive terms.

$$V_{ij} = f_c(r_{ij})[f_R(r_{ij}) + b_{ij}f_A(r_{ij})] \quad (\text{B.7})$$

where r_{ij} is the distance between atoms i and j , the length of the ij bond.

The functions f_R and f_A represent, respectively, the repulsive and attractive interactions:

$$f_R(r_{ij}) = A_{ij} \exp(-\lambda_{ij}r_{ij}) \quad (\text{B.8})$$

$$f_A(r_{ij}) = -B_{ij} \exp(-\mu_{ij}r_{ij}) \quad (\text{B.9})$$

Here, f_C is a cutoff function that goes smoothly to zero between two distances R and S , see also Fig. 3.4:

$$f_C(r_{ij}) = \begin{cases} 1, & r_{ij} < R_{ij} \\ \frac{1}{2} + \frac{1}{2} \cos[\pi(r_{ij} - R_{ij})/(S_{ij} - R_{ij})], & R_{ij} < r_{ij} < S_{ij} \\ 0, & r_{ij} > S_{ij} \end{cases} \quad (\text{B.10})$$

The parameter function b_{ij} is a *bond order* term that determines the strength of the attractive interaction:

$$b_{ij} = \chi_{ij} (1 + \beta_i^{n_i} \zeta_{ij}^{n_i})^{-1/2n_i} \quad (\text{B.11})$$

$$\zeta_{ij} = \sum_{k \neq i, j} f_C(r_{ik}) g(\theta_{ijk}) \quad (\text{B.12})$$

$$g(\theta_{ijk}) = 1 + c_i^2/d_i^2 - c_i^2/[d_i^2 + (h_i - \cos\theta_{ijk})^2] \quad (\text{B.13})$$

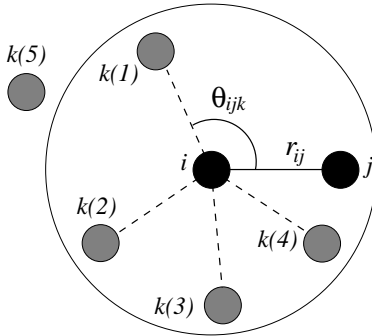


Figure B.1: Schematic draw of a 7 atoms system. b_{ij} term depend on r_{ik} distances and on θ_{ijk} angles. For $r_{ik} > S_{ij}$, i. e. for k atoms outside the cut-off, the b_{ij} term goes to zero. Only first neighbors interactions are computed.

where θ_{ijk} is the angle between ij and ik bonds, see Fig. B.1.

The parameters depend on the atom type. for atoms i and j (of different chemical types), these parameters are

$$\lambda_{ij} = (\lambda_i + \lambda_j)/2, \quad \mu_{ij} = (\mu_i + \mu_j)/2 \quad (\text{B.14})$$

$$A_{ij} = (A_i A_j)^{1/2}, \quad B_{ij} = (B_i B_j)^{1/2}, \quad R_{ij} = (R_i R_j)^{1/2}, \quad S_{ij} = (S_i S_j)^{1/2} \quad (\text{B.15})$$

where the parameters with single index describe the interaction between atoms of the same type. A_{ij} , B_{ij} , λ_{ij} , and μ_{ij} are all positive parameters, with $\lambda_{ij} > \mu_{ij}$.

For interactions between atoms of type m , there are eleven parameters to be fitted: A_m , B_m , λ_m , μ_m , R_m , S_m , β_m , n_m , c_m , d_m , and h_m .

The parameter χ takes into account the strengthening or weakening of heteropolar bonds, relative to the value obtained by simple interpolation. Thus any ‘chemistry’ is included in this parameter. For single component, $\chi_{ii} = 1$.

Table B.1 gives the set of parameters for silicon [24], carbon [24], and nitrogen [60] used in this work. Fig. B.2 shows the term V_{ij} for such interactions, where only atoms pairs are considered. The steep annihilation

lation of $V_{ij}(r_{ij})$ for $R_{ij} < r_{ij} < S_{ij}$ is due to the cutoff function f_C the behavior of which, for carbon interactions, is shown in Fig. 3.4. The cutoff values R_{ij} and S_{ij} are chosen to include only first neighbors.

Table B.1: Parameters for silicon [24], carbon [24], and nitrogen [60] to be used in the Tersoff equations.

	Si	C	N
$A(eV)$	1830.8	1393.6	6368.14
$B(eV)$	471.18	346.7	511.760
$\lambda(\text{\AA}^{-1})$	2.4799	3.4879	5.43673
$\mu(\text{\AA}^{-1})$	1.7322	2.2119	2.70000
β	1.1000×10^{-6}	1.5724×10^{-7}	5.2938×10^{-3}
c	100390	38049	20312.0
d	16.217	4.384	25.5103
h	-0.59825	-0.57058	-0.56239
R	2.7	1.8	1.8
S	3.0	2.1	2.1
χ	Si-C=0.9776	Si-N=0.65	C-N=1.00

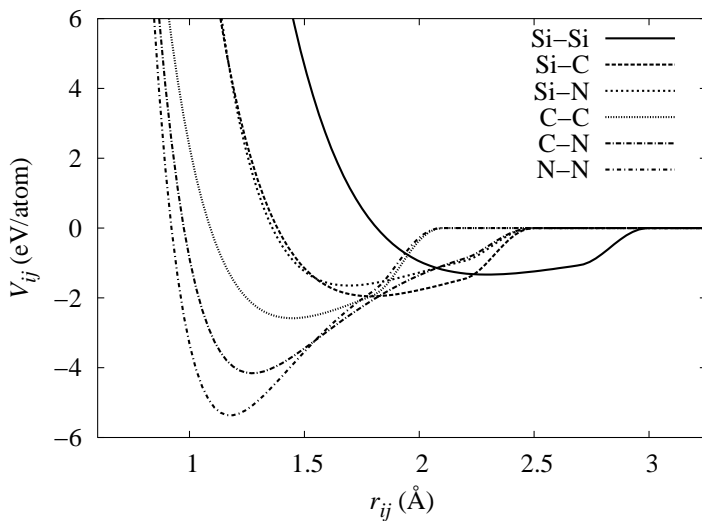


Figure B.2: The pair potential term for Si-Si, Si-C, Si-N, C-C, C-N, and N-N interactions in eV/atom.

List of Figures

2.1	Synthetic path to precursor-derived ceramics.	7
2.2	Ternary Si-C-N composition diagram. (a) compositions on the tie-line C-Si ₃ N ₄ ; (b) compositions in the three-phase field SiC-Si ₃ N ₄ -C; (c) Compositions located in the three-phase field SiC-Si ₃ N ₄ -Si.	9
2.3	Ternary Si-C-N phase diagrams including compositions of ceramics <i>VT50</i> (triangles) and <i>NCP200</i> (rhombs) at $P=1$ atm N ₂ at different temperatures: (a) $1687 \text{ K} < T < 1757 \text{ K}$; (b) $1757 \text{ K} < T < 2114 \text{ K}$; (c) $T > 2114 \text{ K}$. Decomposition of as-pyrolized <i>VT50</i> ceramics above 2114 K occurs in one step delivering SiC/C composites, whereas decomposition of <i>NCP200</i> ceramic proceeds in two steps [10, 28].	14
3.1	Periodic boundary conditions, a two dimensional system. Particles can enter and leave each box across each of the four edges. In a three-dimensional example, particles would be free to cross any of the six cube faces. Particles interact with real and image particles which are within the potential cut-off distance.	17
3.2	Schematic drawing of atoms i with hybridization sp^2 (planar three-fold coordination, left of figure) and with sp^3 hybridization (tetrahedral, four-fold coordination, right of figure).	24
3.3	Tersoff potential between atom i and j (Fig.3.2) when atom i is in two different hybridizations. Atoms i and j are carbon atoms, parameters are taken from Ref. [53]. The abrupt modification of the potential curve for $r > 1.8\text{\AA}$ is due to the presence of the cut-off function displayed in Fig. 3.4.	25
3.4	Cut-off function for the C-C Tersoff potential [53].	25

4.1	Si-C-N concentration diagram, showing the positions of the Si-C-N systems with respect to the quasi-binary lines (dashed) $\text{Si}_3\text{N}_4\text{-C}$ and $\text{Si}_3\text{N}_4\text{-SiC}$	32
4.2	Normalized RDF of the five Si-C-N systems quenched to $T = 0$ K.	32
4.3	Silicon coordination as a function of $\eta = N_{\text{N}}/(N_{\text{Si}} + N_{\text{N}})$. The total silicon coordination number $Z(\text{Si})$ and the partial coordination number $Z(\text{Si})_{\text{N}}$ increase monotonically with η , showing that Si atoms are coordinated to the maximum possible number of N atoms.	34
4.4	Normalized angle distribution functions of bonds originating from silicon atoms.	35
4.5	Normalized angle distribution functions of Si-N-Si bonds originating from nitrogen atoms.	35
4.6	Carbon coordination as a function of $\gamma = N_{\text{C}}/(N_{\text{Si}}^{\text{available}} + N_{\text{C}})$	39
4.7	Normalized angle distribution functions of bonds originating from carbon atoms.	39
4.8	Separation into amorphous C-rich domains in the $S1$ system. Only the carbon atoms are displayed. The cubic simulation box at the end of the simulated annealing has side lengths of 33 Å.	42
4.9	Monoatomic graphitic layers in the $S4$ system. Only the carbon atoms are displayed. The cubic simulation box at the end of the simulated annealing has side lengths of 43 Å.	43
4.10	Potential energy of the system as a function of the temperature	47
4.11	Density of the system as a function of temperature	47
4.12	Diffusion coefficients for silicon, carbon and nitrogen atoms at different temperatures	49
4.13	Arrhenius plot for diffusion coefficients at high temperature. The linear regression was calculated for $T \geq 3900$ K	50

4.14	Partial C-C RDFs at different temperatures	52
4.15	Partial Si-N RDFs at different temperatures	52
4.16	Partial Si-C RDFs at different temperatures	53
4.17	Thermal evolution of $Z(\text{Si})$, $Z(\text{C})$, and $Z(\text{N})$	54
4.18	Normalized ADF of bonds originating from Si atoms	55
4.19	Normalized ADF of Si-N-Si bonds originating from N atoms	55
4.20	Normalized ADF of bonds originating from C atoms	56
4.21	Percentage quantities of CC_3 , NSi_3 , and SiN_4 structures are plotted as a function of the annealing T	57
5.1	Snapshots of the MD supercell during annealing at $T \simeq 0.45 \times T_m$. The dashed line shows the initial c/a in- terface position.	63
5.2	Arrhenius plot of the growth rates.	65
5.3	$GB111$ system before (a) and after (b) the simulated annealing at $T \simeq 0.60 \times T_m$. The dashed lines show the position of the two $\langle 111 \rangle$ tilt grain boundaries ($\Sigma = 3$, (111) , 70.53°) before the annealing.	65
5.4	$GB120$ system before (a) and after (b) the simulated annealing at $T \simeq 0.60 \times T_m$. The dashed lines show the position of the two $\langle 110 \rangle$ tilt grain boundaries ($\Sigma = 9$, (221) , 38.94°) before the annealing. Boxes in (b) surround defects after crystallization.	66
5.5	$GB221$ system before (a) and after (b) the simulated annealing at $T \simeq 0.60 \times T_m$. The initial crystal seed layer contains two $\langle 001 \rangle$ tilt grain boundaries ($\Sigma = 5$ (120) 36.87°). Boxes in (b) surround defects after crystallization.	67
5.6	Schematic draw of the five initial MD supercells. The shadowed region corresponds to the crystalline one.	68
5.7	Normalized melting temperature of the crystal seed as a function of the surface/volume ratio of the seed, Ω	69

5.8	Four MD supercells containing a crystal seed layer in contact with the amorphous layer. Three different crystal orientations leading to seven different c/a interfaces are displayed, (a) {100}-Si and -C, (b) {110}, (c) single-bond {111}-Si and -C, and (d) triple-bond {111}-Si and -C. In this picture, C atoms are dark while Si atoms are light.	71
5.9	72
B.1	Schematic draw of a 7 atoms system. b_{ij} term depend on r_{ik} distances and on θ_{ijk} angles. For $r_{ik} > S_{ij}$, i. e. for k atoms outside the cut-off, the b_{ij} term goes to zero. Only first neighbors interactions are computed.	82
B.2	The pair potential term for Si-Si, Si-C, Si-N, C-C, C-N, and N-N interactions in eV/atom.	84

List of Tables

4.1	Total ($Z(A)$) and partial ($Z(A)_B$) coordination numbers and nitrogen/silicon ratio (η) of the five systems.	33
4.2	Percentages of Si tetrahedra in the different systems, with respect to the total number of silicon atoms.	36
4.3	Percentages of C structures in the different systems, with respect to the total number of carbon atoms.	40
4.4	Entropy factors (D_0) and activation energies (H) for self-diffusion in amorphous Si-C-N	50
4.5	Peak positions of partial RDFs for the amorphous system and relevant crystal phases.	51
4.6	Calculated partial coordination numbers	53
4.7	Percentages of Si, C, and N structures with respect to the total Si, C, and N numbers respectively.	57
B.1	Parameters for silicon [24], carbon [24], and nitrogen [60] to be used in the Tersoff equations.	83

Bibliography

- [1] R. Raj, Fundamental research in structural ceramics for service near 2000°C, *J. Am. Ceram. Soc.* **76** (1993) 2147–2174.
- [2] W. Verbeek and G. Winter, “German Patent 2236078”, (1974).
- [3] S. Yajima, J. Hayashi, M. Omori, and K. Okamura, Development of a silicon-carbide fiber with high-tensile strength, *Nature* **261** (1976) 683.
- [4] R. Riedel, G. Passing, H. Schönfelder, and R. J. Brook, Synthesis of dense silicon-based ceramics at low temperatures, *Nature* **355** (1992) 714–716.
- [5] J. Bill and F. Aldinger, Precursor-Derived covalent ceramics, *Advanced Materials* **7** (1995) 775–787.
- [6] M. Weinmann and F. Aldinger, High temperature stable ceramics from inorganic polymers, in *Precursor-Derived Ceramics* (Edited by J. Bill, F. Wakai, and F. Aldinger), pages 83–92, Weinheim, Germany, (1999), Wiley-VCH Verlag.
- [7] M. Weinmann and F. Aldinger, *Handbook of Advanced Ceramics*, chapter 5, pages 267–370, Elsevier Inc., (2003).
- [8] J. Bill, J. Schuhmacher, K. Müller, S. Schempp, J. Seitz, J. Dürr, H. P. Lamparter, J. Golczewski, J. Peng, H. J. Seifert, and F. Aldinger, Investigations into the structural evolution of amorphous Si-C-N ceramics from precursors, *Z. Metallkd.* **91** (2000) 335–351.
- [9] H.-J. Kleebe, H. Störmer, S. Trassl, and G. Ziegler, Thermal stability of SiCN ceramics studied by spectroscopy and electron microscopy, *Appl. Organometal. Chem.* **15** (2001) 858–866.
- [10] J. Bill, J. Seitz, , G. Thurn, J. Dürr, J. Canel, B. Z. Janos, A. Jalowiecki, D. Sauter, S. Schempp, H. P. Lamparter, J. Mayer, and F. Aldinger, Structure analysis and properties of Si-C-N ceramics derived from polysilazanes, *Phys. Stat. Sol. (a)* **166** (1998) 269–296.
- [11] H.-J. Kleebe, Microstructure and stability of polymer-derived ceramics; the si-c-n system, *Phys. Stat. Sol. (a)* (1998).

- [12] Y. Iwamoto, W. Völger, E. Kroke, R. Riedel, T. Saitou, and K. Matsunaga, Crystallization behavior of amorphous silicon carbonitride ceramics derived from organometallic precursors, *J. Am. Ceram. Soc.* **84** (2001) 2170–2178.
- [13] H.-J. Kleebe, D. Suttor, H. Müller, and G. Ziegler, Decomposition-crystallization of polymer-derived Si-C-N ceramics, *J. Am. Ceram. Soc.* **81** (1998) 2971–2977.
- [14] L. L. Snead and S. J. Zinkle, Structural relaxation in amorphous silicon carbide, *Nucl. Instrum. Meth. Phys. Res. B* **191** (2002) 497.
- [15] R. Riedel and M. Seher, Crystallization behaviour of amorphous silicon nitride, *J. Eur. Ceram. Soc.* **7** (1991) 21.
- [16] J. Haug, P. Lamparter, M. Weinmann, and F. Aldinger, Diffraction study on the atomic structure and phase separation of amorphous ceramics in the Si-(B)-C-N system. 1. Si-C-N ceramics, *Chemistry of Materials* **16** (2004) 72–82.
- [17] J. A. Golczewski and F. Aldinger, Thermodynamic modeling of amorphous Si-C-N ceramics derived from polymer precursors, *Journal of Non Crystalline Solids* **347** (2004) 204–210.
- [18] S. Trassl, G. Motz, E. Rössler, and G. Ziegler, Characterization of the free-carbon phase in precursor-derived Si-C-N ceramics: I, spectroscopic methods, *J. Am. Ceram. Soc.* **85** (2002) 239–244.
- [19] S. Trassl, H.-J. Kleebe, H. Störmer, G. Motz, E. Rössler, and G. Ziegler, Characterization of the free-carbon phase in Si-C-N ceramics: Part II, comparison of different polysilazane precursors, *J. Am. Ceram. Soc.* **85** (2002) 1268–1274.
- [20] S. Schempp, J. Dürr, P. Lamparter, J. Bill, and F. Aldinger, Study of the atomic structure and phase separation in amorphous Si-C-N ceramics by x-ray and neutron diffraction, *Z. Naturforsch.* **53 a** (1998) 127–133.
- [21] J. Dürr, P. Lamparter, J. Bill, S. Steeb, and F. Aldinger, An x-ray and neutron scattering investigation of precursor derived $\text{Si}_{24}\text{C}_{43}\text{N}_{33}$ ceramics, *Journal of Non Crystalline Solids* (1998).

- [22] J. Haug, *Untersuchung der Struktur und des Kristallisationsverhaltens von Si-C-N- und Si-B-C-N-Prekursorkeramiken mit Röntgen- und Neutronbeugung*, Ph.D. thesis, Max Planck Institut für Metallforschung, Stuttgart, (2002).
- [23] J. Tersoff, New empirical model for the structural properties of silicon, *Phys. Rev. Lett.* **56** (1986) 632–635.
- [24] J. Tersoff, Modeling solid state chemistry: Interatomic potentials for multicomponent systems, *Phys. Rev. B* **39** (1989) 5566–5568.
- [25] N. Resta, C. Kohler, and H.-R. Trebin, Molecular dynamics simulations of amorphous Si-C-N ceramics: Composition dependence of the atomic structure, *J. Am. Ceram. Soc.* **86** (2003) 1409–1414.
- [26] N. Resta, C. Kohler, and H.-R. Trebin, Modeling the crystal growth of cubic silicon carbide by molecular dynamics simulations, *Mat. Res. Soc. Symp. Proc.* **742** (2003).
- [27] A. Bauer, M. Christ, A. Zimmermann, and F. Aldinger, Fracture toughness of amorphous precursor-derived ceramics in the silicon-carbon-nitrogen system, *J. Am. Ceram. Soc.* **84** (2001) 2203–2207.
- [28] H. J. Seifert, J. Peng, H. L. Lukas, and F. Aldinger, Phase equilibria and thermal analysis of Si-C-N ceramics, *Journal of Alloys and Compounds* **320** (2001) 251–261.
- [29] R. Riedel, H.-J. Kleebe, H. Schönfelder, and F. Aldinger, A covalent Micro/nano-Composite resistant to high-temperature oxidation, *Nature* **374** (1995) 526–528.
- [30] R. Raj, L. An, S. Shah, R. Riedel, C. Fasel, and H.-J. Kleebe, Oxidation kinetics of an amorphous silicon carbonitride ceramic, *J. Am. Ceram. Soc.* **84** (2001) 1803–1810.
- [31] E. Butchereit, K. G. Nickel, and A. Müller, Precursor-derived Si-B-C-N ceramics: Oxidation kinetics, *J. Am. Ceram. Soc.* **84** (2001) 2184–2188.
- [32] A. Rendtel, H. Hübner, M. Hermann, and C. Schubert, Silicon nitride/silicon carbide nanocomposite materials: II, hot strength, creep, and oxidation resistance, *J. Am. Ceram. Soc.* **81** (1998) 1109–1120.

- [33] R. Riedel, L. M. Ruswisch, L. An, and R. Raj, Amorphous siliconboron carbonitride ceramic with very high viscosity at temperatures above 1500°C, *J. Am. Ceram. Soc.* **81** (1998) 3341–3344.
- [34] G. Thurn, J. Canel, J. Bill, and F. Aldinger, Compression creep behavior of precursor-derived Si-C-N ceramics, *J. Eur. Ceram. Soc.* **19** (1999) 2317–2323.
- [35] S. R. Shah and R. Raj, Nanoscale densification and creep in polymer-derived silicon carbonitrides at 1350°C, *J. Am. Ceram. Soc.* **84** (2001) 2208–2212.
- [36] A. Zimmermann, A. Bauer, M. Christ, Y. Cai, and F. Aldinger, High-temperature deformation of amorphous Si-C-N and Si-B-C-N ceramics derived from polymers, *Acta Materialia* **50** (2002) 1187–1196.
- [37] J. Bill and F. Aldinger, Progress in materials synthesis, *Z. Metallkd.* **87** (1996) 827.
- [38] R. Riedel, A. Kienzle, W. Dressler, L. Ruwisch, J. Bill, and F. Aldinger, A siliconboron carbonitride ceramic stable to 2000°C, *Nature* **382** (1996) 796–798.
- [39] F. Aldinger, M. Weinmann, and J. Bill, Precursor-derived Si-B-C-N ceramics, *Pure and Applied Chemistry* **70** (1998) 439–448.
- [40] M. Christ, G. Thurn, M. Weinmann, J. Bill, and F. Aldinger, High-temperature mechanical properties of Si-B-C-N precursor-derived amorphous ceramics and the applicability of deformation models developed for metallic glasses, *J. Am. Ceram. Soc.* **83** (2000) 3025–32.
- [41] J. Bill, T. W. Kamphowe, A. Müller, T. Wichmann, A. Zern, A. Jalowieki, J. Mayer, M. Weinmann, J. Schuhmacher, K. Müller, J. Peng, H. J. Seifert, and F. Aldinger, Precursor-derived Si-(B-)C-N ceramics: thermolysis, amorphous state and crystallization, *Applied Organometallic Chemistry* **15** (2001) 777–793.
- [42] Z. C. Wang, F. Aldinger, and R. Riedel, Novel silicon-boron-carbon-nitrogen materials thermally stable up to 2200°C, *J. Am. Ceram. Soc.* **84** (2001) 2179–2183.

- [43] M. Höerz, A. Zern, F. Berger, J. Haug, K. Müller, F. Aldinger, and M. Weinmann, Novel polysilazanes as precursors for silicon nitride/silicon carbide composites without free carbon, *J. Eur. Ceram. Soc.* **25** (2005) 99–110.
- [44] L. An, R. Riedel, C. Konetschny, H.-J. Kleebe, and R. Raj, Newtonian viscosity of silicon carbonitride at high temperature, *J. Am. Ceram. Soc.* **81** (1998) 1349–1352.
- [45] T. Nishimura, R. Haug, J. Bill, G. Thurn, and F. Aldinger, Mechanical and thermal properties of Si-C-N material from polyvinylsilazane, *Journal of Material Science* **33** (1998) 5237.
- [46] A. Saha, R. Raj, D. L. Williamson, and H.-J. Kleebe, Characterization of nanodomains in polymer-derived SiCN ceramics employing multiple techniques, *J. Am. Ceram. Soc.* **88** (2005) 232–234.
- [47] R. Riedel, M. Seher, J. Mayer, and D.-V. Szabó, Polymer-derived Si-based bulk ceramics, part I: Preparation, processing and properties, *J. Eur. Ceram. Soc.* **15** (1995) 703.
- [48] J. Stadler, R. Mikulla, and H.-R. Trebin, IMD: A software package for molecular dynamics studies on parallel computers, *Int. J. Mod. Phys. C* **8** (1997) 1131–1140.
- [49] J. Roth, IMD - a molecular dynamics program and applications, in *Proceedings of the Workshop on Molecular Dynamics on Parallel Computers* (Edited by J. G. R. Esser, P. Grassberger and M. Lawrenz), page 83. World Scientific - Singapore, (2000).
- [50] <http://www.itap.physik.uni-stuttgart.de/~imd>
- [51] J. Tersoff, New empirical model for the structure and energy of covalent systems, *Phys. Rev. B* **37** (1988) 6991–7000.
- [52] J. Tersoff, Empirical interatomic potential for silicon with improved elastic properties, *Phys. Rev. B* **38** (1988) 9902–9905.
- [53] J. Tersoff, Empirical interatomic potential for carbon, with applications to amorphous carbon, *Phys. Rev. Lett.* **61** (1988) 2879–2882.
- [54] D. Frenkel and B. Smit, *Understanding Molecular Simulation*, Academic Press, (1996).

- [55] R. Biswas and D. R. Hamann, Interatomic potentials for silicon structural energies, *Phys. Rev. Lett.* (1985).
- [56] F. H. Stillinger and T. A. Weber, Computer-simulation of local order in condensed phases of silicon, *Phys. Rev. B* **31** (1985) 5262–5271.
- [57] P. N. Keating, Effect of invariance requirements on elastic strain energy of crystals with application to diamond structure, *Phys. Rev.* **145** (1966) 637.
- [58] D. B. Boercker, Constant-pressure simulation of carbon in the bc8 structure, *Phys. Rev. B* **44** (1991) 11592–11596.
- [59] M. Ishimaru, K. Yoshida, and T. Motooka, Application of empirical interatomic potentials to liquid si, *Phys. Rev. B* **53** (1996) 7176–7181.
- [60] F. de Brito Mota, J. F. Justo, and A. Fazzio, Structural properties of amorphous silicon nitride, *Phys. Rev. B* **58** (1998) 8323–8328.
- [61] K. Matsunaga, Y. Iwamoto, C. A. J. Fisher, and H. Matsubara, Molecular dynamics study of atomic structures in amorphous Si-C-N ceramics, *Journal of the Ceramic Society of Japan* **107** (1999) 1025–1031.
- [62] M. Amkreutz and T. Frauenheim, Understanding precursor-derived amorphous Si-C-N ceramics on the atomic scale, *Phys. Rev. B* **65** (2002) 134113[1–9].
- [63] P. Kroll, Modelling polymer-derived ceramics, *J. Eur. Ceram. Soc.* **25** (2005) 163–174.
- [64] M. Seher, J. Bill, R. Riedel, and F. Aldinger, Processing and properties of carbon containing silicon nitride ceramics derived from the pyrolysis of polyhydrido-chlorosilazanes, *Key Eng. Mater.* **89-91** (1994) 101.
- [65] J. Bill, Private communication, (2002).
- [66] J. Dürr, *Struktur von amorphen Siliziumcarbonitrid-keramiken mit hilfe von Röntgen- und Neutronenstreu-untersuchungen und Isotopensubstitution*, Ph.D. thesis, University of Stuttgart, (1997).

- [67] S. Matics and W. F. J. Frank, Diffusion of ^{71}Ge in the amorphous ceramic $\text{Si}_{28}\text{C}_{36}\text{N}_{36}$, *J. Non Crystalline Solids* (2000).
- [68] S. Matics, *Selbst- und Fremddiffusion in amorphem $\text{Si}_{28}\text{C}_{36}\text{N}_{36}$ und Si_3N_4* , Ph.D. thesis, Max Planck Institut für Metallforschung and Institut für Theoretische und Angewandte Physik, University of Stuttgart, (2000).
- [69] L.-T. Voss, *Diffusion in amorphen Vorstufen von Si-(B)-C-N Keramiken und verwandten Materialien*, Ph.D. thesis, Max Planck Institut für Metallforschung and University of Stuttgart, (2002).
- [70] F. P. Bundy, H. T. Hall, H. M. Strong, and R. H. Wentorf, Man-made diamonds, *Nature* **176** (1955) 51.
- [71] T. Motooka, K. Nisihira, S. Munetoh, K. Moriguchi, and A. Shintani, Molecular-dynamics simulations of solid-phase epitaxy of Si: Growth mechanisms, *Phys. Rev. B* **61** (2000) 8537–8540.
- [72] R. Pampuch and L. Stoibierski, Morphology of silicon carbide formed by chemical vapor deposition, *Ceram. Int.* **3** (1977) 43–52.
- [73] B. Wessels, H. C. Gatos, and A. F. Witt, in *Proc. 3^d Intern. Conf. Silicon Carbide*, page 25, Miami, (Sept. 1973).
- [74] M. Christ, A. Zimmermann, A. Zern, M. Weinmann, and F. Aldinger, High temperature deformation behavior of crystallized precursor-derived Si-B-C-N ceramics, *Journal of Material Science* **36** (2001) 5767.
- [75] K. Matsunaga and Y. Iwamoto, Molecular dynamics study of atomic structure and diffusion behavior in amorphous silicon nitride containing boron, *J. Am. Ceram. Soc.* **84** (2001) 2213–2219.
- [76] Y. Cai, A. Zimmermann, S. Prinz, and F. Aldinger, Crystallization behavior of polymer-derived Si-B-C-N ceramics in a high-pressure nitrogen environment, *Journal of Materials Research* **17** (2002) 2765–2767.
- [77] A. Müller, J. Q. Peng, H. J. Seifert, J. Bill, and F. Aldinger, Si-B-C-N ceramic precursors derived from dichlorodivynylsilane and chlorotrivinylsilane. 2. Ceramization of polymers and high-temperature behavior of ceramic materials, *Chemistry of Materials* **14** (2002) 3406–3412.

- [78] J. Peng, *Thermochemistry and Constitution of Precursor-Derived Si-B-C-N Ceramics*, Ph.D. thesis, Institut für Nichtmetallische Anorganische Materialien der Universität Stuttgart and Max-Planck Institut für Metallforschung (Stuttgart), Pulvermetallurgisches Laboratorium, (2002).
- [79] N. Janakiraman, M. Weinmann, J. Schuhmacher, K. Muller, J. Bill, F. Aldinger, and P. Singh, Thermal stability, phase evolution, and crystallization in Si-B-C-N ceramics derived from a polyborosilazane precursor, *J. Am. Ceram. Soc.* **85** (2002) 1807–1814.
- [80] A. Müller, A. Zern, P. Gerstel, J. Bill, and F. Aldinger, Boron-modified poly(propenylsilane)-derived Si-B-C-N ceramics: preparation and high temperature properties, *J. Eur. Ceram. Soc.* **22** (2002) 1631–1643.
- [81] N. V. R. Kumar, R. Mager, Y. Cai, A. Zimmermann, and F. Aldinger, High temperature deformation behavior of crystallized Si-B-C-N ceramics obtained from a boron modified poly(vinyl)silazane polymeric precursor, *Scripta Materialia* **51** (2004) 65–69.
- [82] J. Haug, P. Lamparter, M. Weinmann, and F. Aldinger, Diffraction study on the atomic structure and phase separation of amorphous ceramics in the Si-(B)-C-N system. 2. Si-B-C-N ceramics, *Chemistry of Materials* **16** (2004) 83–92.
- [83] N. Janakiraman, A. Zern, M. Weinmann, F. Aldinger, and P. Singh, Phase evolution and crystallization in Si-B-C-N ceramics derived from a polyborosilazane precursor: microstructural characterization, *J. Eur. Ceram. Soc.* **25** (2005) 509–520.

Acknowledgments

This work was performed in the time between April 2000 and March 2003 at the Institut für Theoretische und Angewandte Physik, University of Stuttgart, in the group of Prof. H.-R. Trebin, and at the Max-Planck-Institut für Metallforschung, in the department of Prof. F. Aldinger. During the period I spent in Stuttgart many people helped me in my work, in particular I would like to thank:

- Prof. Hans-Rainer Trebin for accepting me in his institute, for his continuous guidance and supervision throughout my work as well as for the friendly working atmosphere he creates in his group.
- Prof. Fritz Aldinger for giving me the opportunity to work in his department and to participate to very fruitful internal group meetings at the Schloß Ringberg. I am grateful to him also for taking over the *Mitbericht*.
- Prof. Manfred Rühle for having accepted me as member of the "Graduiertenkolleg für Innere Grenzflächen", which gave me the opportunity to widen my knowledge in the field of material science.
- Prof. Eric Mittemeijer for taking over the *Mitprüfung*.
- Dr. Christopher Kohler for his help with the computer programming, as well as his kindness and promptness in helping with the simulations. I am grateful to him also for the translation of the extended abstract in German.
- all my colleagues at the ITAP, in particular Uli Koschella for his friendly and professional help with the computer facilities, Christoph Rudhart and Michael Reichenstein for their help in solving all kind of problems.
- the people from PML, in particular Dr. Joachim Bill for helpful support and scientific discussions, Dr. Anita Müller for the technical revision of the *Zusammenfassung*, and Mrs. Sabine Paulsen for her kindness and promptness in solving bureaucratic problems.
- my family: my parents Bettina and Raffaele for their continuous encouragement, my daughter Camilla for the joy she brings, and my husband Stefano who kept me holding on throughout this time and without whom the conclusion of this work would not have been possible.

This project has been financially supported by the Deutsche Forschungsgemeinschaft (DFG) within the Graduiertenkolleg "Innere Grenzflächen in kristallinen Materialien" (GRK 285).

Curriculum Vitae

Name: Nicoletta Resta
Date of birth: July 19th, 1973
Place of birth: Genova, Italy
Nationality: Italian
Marital status: married, one child
born in Trieste (Italy), June 8th, 2003

1987–1992 Liceo Scientifico G. Oberdan, Trieste, Italy
7/1992 Maturità Scientifica
1992–1994 Undergraduate student in the faculty of Medicine,
University of Trieste, Italy
1994–1999 Undergraduate student in the faculty of Chemistry,
University of Trieste, Italy
1998–2000 Undergraduate thesis work in the Department
of Biochemistry, Biophysics, and Macromolecular
Chemistry. Title of the thesis: *Glass Transition and
Enthalpy Relaxation of Oligosaccharides: Calorimetric
and Molecular Dynamics Studies on Lactose and Sucrose*
3/2000 Laurea in Chimica, full marks *cum laude*
4/2000–3/2003 PhD student at the Max Planck Institut für
Metallforschung, Stuttgart, Germany.
2/2004 – 3/2005 Scientific administration for the Project NAPOLY
*Possibilities through Advancements in Nanotechnology
for Development of High Value Eco-Friendly New
Biopolymers and their Applications*, a Specific Support
Action of the European Community.
9/2004 – 1/2005 Information and training for high schools students
within the project *Doing science with computers*
of the Democritos Modeling Centre for Research in
Atomistic Simulations, Trieste, Italy